Lab on a Chip

Single-cell microfluidic impedance cytometry: from raw signals to cell phenotypes using data analytics

Journal:	*Lab on a Chip*
Manuscript ID	LC-TRV-08-2020-000840.R1
Article Type:	Tutorial Review
Date Submitted by the Author:	29-Oct-2020

Complete List of Authors:	Honrado, Carlos; University of Virginia Bisegna, Paolo; University of Rome Tor Vergata, Department of Civil Engineering and Computer Science Swami, Nathan; University of Virginia, Electrical and Computer Engineering Caselli, Federica; University of Rome Tor Vergata, Department of Civil Engineering and Computer Science

ARTICLE

Single-cell microfluidic impedance cytometry: from raw signals to cell phenotypes using data analytics

Received 00th January 20xx,
Accepted 00th January 20xx

DOI: 10.1039/x0xx00000x

Carlos Honrado,[a] Paolo Bisegna,[b] Nathan S. Swami *[a] and Federica Caselli *[b]

The biophysical analysis of single-cells by microfluidic impedance cytometry is emerging as a label-free and high-throughput means to stratify the heterogeneity of cellular systems based on their electrophysiology. Emerging applications range from fundamental life-science and drug assessment research to point-of-care diagnostics and precision medicine. Recently, novel chip designs and data analytic strategies are laying the foundation for multiparametric cell characterization and subpopulation distinction, which are essential to understand biological function, follow disease progression and monitor cell behaviour in microsystems. In this tutorial review, we present a comparative survey of the approaches to elucidate cellular and subcellular features from impedance cytometry data, covering the related subjects of device design, data analytics (*i.e.*, signal processing, dielectric modelling, population clustering), and phenotyping applications. We give special emphasis to the exciting recent developments of the technique (timeframe 2017-2020) and provide our perspective on future challenges and directions. Its synergistic application with microfluidic separation, sensor science and machine learning can form an essential toolkit for label-free quantification and isolation of subpopulations to stratify heterogeneous biosystems.

1 Introduction

Cellular systems exhibit a wide degree of heterogeneity[1,2], likely due to temporal fluctuations in the levels of regulatory proteins, position in the cell cycle and the activation of cell death mechanisms. These heterogeneous subpopulations can fundamentally affect biological function and determine disease presentation, progression and treatment response[3]. Quantifying phenotypic heterogeneity is particularly important, since it represents active changes to the cell under external interventions or micro-environment alterations.

The state-of-the-art method for quantifying phenotypic heterogeneity is by fluorescence-based flow cytometry, wherein the characteristic surface proteins expressed by cells are labelled using fluorescent antibody receptors and measured at high throughput (10^3-10^4 cells/s) under laser excitation to obtain multi-dimensional data. However, quantification by this technique is infeasible in several scenarios, such as when the expressed cell surface proteins may not reliably identify cells of interest (*e.g.* stem cells[4–7]); when the measured phenotype exhibits spatial complexity (*e.g.* mitochondrial features[8]) or unknown intensity thresholds (*e.g.* metabolism[9]). Other limiting scenarios include the need to repeatedly analyse the same set of cells (*e.g.* kinetic monitoring under drug interventions[10]); or when cell labelling affects its functionality or the staining process involves costly chemicals and time-consuming tasks. In these cases, which are forming an increasing proportion of cell phenotypic studies of relevance to diseases, there is much interest in complementary methods for biophysical analysis of single-cells[11], preferably using label-free metrics that are based on inherent cell properties, to enable phenotypic quantification from heterogeneous samples and to trigger downstream cell isolation strategies.

Phenotypic heterogeneity is often assessed based on measurable differences in biophysical properties, such as cell size, shape, deformability and subcellular characteristics, including membrane composition and morphology, mitochondrial network, organelles in cytoplasm, ion pile-up in endoplasmic reticulum and nucleus size. Such cell phenotype changes can be influenced by genetic and/or proteomic factors, as well as by the extracellular matrix and by active environmental cues. Fluorescence cytometry, while highly sensitive to biochemical phenotypes, is not well suited to discern biophysical phenotypes. On the other hand, the emerging frontier of cell biophysical characterization can be achieved by means of impedance cytometry (Fig. 1). In fact, biophysical phenotypes can be assessed by fitting single-cell impedance cytometry data to appropriate dielectric models, thereby enabling the quantification and stratification of complex samples in a label-free multi-parametric manner.

Microfluidic impedance cytometry involves the measurement of the electric field screening of individual cells passing over patterned electrodes in a microchannel, as accomplished by electric current variation under an applied AC voltage (Fig. 1A). The measured current exhibits a characteristic temporal signal shape (Fig. 1B-C) whose features depend on: the applied potential, the system impedance, and cell properties, *i.e.* volume and dielectric properties[12]. The measured impedance is frequency dependent and exhibits characteristic dispersions for

[a] *Department of Electrical and Computer Engineering, University of Virginia, Charlottesville, VA 22904, USA.*
[b] *Department of Civil Engineering and Computer Science, University of Rome Tor Vergata, Via del Politecnico 1, 00133 Rome, Italy.*

each subcellular region[13] (Fig. 1F). While the electrical double-layer around the electrodes screens the field at frequencies < 100 kHz, the signal is chiefly determined by the cellular electrical size in the 0.1-1 MHz range due to complete membrane-induced screening. Polarization of the plasma membrane in the 2-10 MHz range offers information on membrane morphology based on measured capacitance. In the 10-30 MHz range, the membrane is minimally polarized, so that the cytoplasmic conductivity and permittivity provide information on the organelles, while at higher frequencies, the response is dependent on nucleus properties. It is noteworthy that the exact frequency range values are dependent on cell size, media conductivity and the complex conductivity of the respective subcellular layer (see also Box 2 in Section 3). Using superimposed voltage sinusoids the impedance magnitude and phase (Fig. 1D) can be obtained simultaneously over multiple frequencies for each cell, paving the way for multiparametric analysis by fitting impedance spectra to the appropriate shell model[14,15] (Fig. 1G) for characterization of subcellular electrophysiology. However, while cell recognition by fluorescence cytometry can simply be determined based on pre-set thresholds, recognition based on impedance metrics requires the analysis of temporal signal trains of single cells at each frequency and population-level analysis of the scatter plots (Fig 1E) to identify characteristic frequency dispersions (Fig. 1F).

A number of reviews with broad scope include a discussion on microfluidic impedance cytometry (*e.g.*, refs.[16–24]). For a comprehensive description of the basic principles of microfluidic impedance cytometry and the relevant literature from early works to 2010, the reader is referred to the review papers by Cheung *et al.*[25] and Sun and Morgan[13]. Subsequent developments were reviewed by Chen *et al.*[26] in 2015 and by Petchakup *et al.*[27] in 2017. In particular, Chen *et al.* discussed systems with enhanced sensitivity, systems coupled with optical flow cytometry, and point-of-care systems, whereas Petchakup *et al.* reviewed common designs and provided an overview of biomedical applications of the technique. The specific topic of positional dependence and position detection of particles and cells has been recently reviewed by Daguerre et al.[28]

The present review covers the exciting developments that have been achieved in recent years (2017-2020), with a focus on phenotypic elucidation based on signal processing, cell modelling and population-level data analysis. Microfluidic impedance cytometry has evolved from the standard approaches towards novel designs and strategies that greatly enhance the sensitivity and accuracy of the measurements, as well as the information content embedded in the electrical fingerprints, thus enabling multiparametric cell characterization. Furthermore, hybrid platforms combining microfluidic impedance cytometry with other sensing or manipulation modalities have been developed, and device portability has been pursued via system integration, simplified fabrication and real-time processing. Overall, this opens up new opportunities in fundamental and applied research, with biophysical cell phenotyping of complex samples becoming increasingly important. It is our intention to provide the reader with an overview of such current research efforts.

On the other hand, the evolution from classical analysis based on signal amplitude at limited bandwidth, towards accurate multiparametric characterization at high-throughput, calls for tailored strategies of signal processing and data analysis to elucidate cell phenotypes from impedance cytometry data. Accordingly, this review has two main tutorial goals: i) to provide a cohesive overview of how high-content single-cell electrical fingerprints are collected and processed; ii) to elucidate the strategies to identify sub-populations of cells based on dielectric modelling and population-level analytics on the collected data to enable statistically relevant inferences on cell phenotype. We provide a systematic review on the emerging approaches to impedance-based cell phenotyping, so that future studies can focus on its standardization and make it more amenable to inline cell recognition for triggering of downstream sorting.

The overall structure of the paper is as follows: Section 2 focuses on device designs for high content signal acquisition, Section 3 deals with data analytics tools to extract the information embedded in the electrical fingerprints, and Section 4 presents a survey of recent cell phenotyping applications. Finally, in Section 5 we draw our view on the perspectives of the technique.

2 Device designs for high-content measurement of single-cell electrical fingerprints

After general guidelines, we briefly review the classic electrode configurations. Then we describe innovative chip designs to obtain increased accuracy and multiparametric cell characterization, as well as platforms with multiple electrical sensing zones and hybrid platforms.

2.1 General considerations

Measurement setup. The most common experimental setup for electrical impedance analysis of single cells is as follows[29]. AC excitation signals at different frequencies are superimposed and applied to the stimulation electrodes, to establish an electric field in the channel, which is filled with a conductive fluid. The electrical current (or currents) determined from measurement electrodes that are maintained at virtual ground is conditioned and demodulated by lock-in amplifiers that provide the in-phase (real) and out-of-phase (imaginary) signals at each frequency, whilst rejecting noise at the other frequencies. Fluidic pumps (syringe pumps, pressure controllers, or peristaltic pumps) are used to establish and regulate the sample flow. As single-cell streamlines pass through the channel, a variation in the measured currents is recorded, which depends on the intrinsic field screening properties of each cell at that frequency. A technique based on maximum length sequences has also been proposed to perform broadband single cell impedance spectroscopy in a short interval of time[30,31].

Sensitivity. The sensitivity is governed by the dimensions of the sensing volume[32]. Traditionally, channels or pores with dimensions comparable to single-cell diameters have been utilized to maximize the detected signal[33]. However, a small volume may lead to practical issues, including tight fabrication tolerances and clogging, or may expose mechanically sensitive cells to high shear stress. In order to maintain high signal-to-noise ratio (SNR) while using relatively large sensing volumes, dielectric focusing can be considered, wherein an insulating fluid is used to hydrodynamically focus a sample stream of particles suspended in electrolyte[32,33]. The SNR also increases with the excitation voltage. However, increasing the voltage may lead to electrochemical reactions at the electrodes, thus causing corrosion and/or bubble formation, especially at low frequency in high conductivity media[34]. Electric-field induced cell damage and loss of viability should also be prevented. Typically in microfluidic impedance cytometry, voltages from fractions of a Volt to a few Volts are adopted, depending on channel geometry, medium conductivity and flow rate (cf. also Table 2 in Section 4).

Frequency range. Probing cells over a broad frequency range is key to cell phenotyping, since different subcellular features can respond within critical frequency ranges, as determined by their dielectric properties. However, at low frequencies (<0.1 MHz) Faradaic reactions at metal electrodes may occur, causing corrosion. Moreover, a double-layer capacitance forms over metal-based electrodes, which dominates the signal at DC and at low frequencies, thus reducing the SNR. The lowest stimulation frequency (*e.g.*, 0.5 MHz) is typically a compromise between the need for sensitivity to cell size versus the need to enhance SNR[25,35]. On the other hand, at high frequencies, the presence of stray capacitances in parallel with the measurement sample will shunt the channel impedance and affect the device sensitivity[36]. Tailored acquisition systems may be needed to maintain high sensitivity at frequency as high as 500 MHz[37]. Microwave based solutions are being developed[38,39] to perform impedance based characterization in the GHz range, which offers direct intracellular permittivity probing, due to electric fields penetrating through the cellular membrane. As each cell exhibits characteristic differences in the water content, nucleus volumetric ratio, protein concentration, or cytoplasm structure, the cellular permittivity measured at high frequencies can be used to enhance the resolution in label-free discrimination between different cells.

Suspension medium. The dielectric properties of the suspension medium can be optimized to modulate the degree and frequency range for passage of field lines through the particle versus the media. Typically, 1x PBS solutions are used, whose formulation is tuned to achieve an optimal conductivity. Lowering suspending media to 0.5x or less[40,41] can enhance field penetration to more interior regions of the cell in the usual operating range (0.5-50 MHz), thus emphasizing differences in subpopulations, but at the cost of increasing measurement noise due to voltage drops from the system impedance. Additional components may be added to the buffer (*e.g.*, sucrose, BSA) to match the density and osmolarity of the suspension medium to that of the suspended particles, thus reducing sedimentation and cell shrinkage or swelling. Pre-coating of the microchannel with proteins is useful to avoid cell sticking to the channel walls.

Throughput. The acquisition throughput of a microfluidic impedance cytometer (*i.e.*, the number of single-cell measurement events per unit time) is generally in the order of a few hundreds of cells per second. This throughput results from the product of flow rate and sample concentration. The higher the flow rate, the shorter the particle transit times, thereby broadening the bandwidth of measured signals. The inverse transit time has to be within the bandwidth of the acquisition system and also sufficiently smaller than the lowest stimulation frequency. Sample concentration is limited by the coincidence issue[42,43] (*i.e.*, two or more particles simultaneously present in the sensing zone). The probability of coincidence depends on the expected number μ of particles in the sensing zone, given by the product of sample concentration and sensing zone volume[44]. In order to keep the probability of coincidences below 10%, the parameter μ has to be kept below 0.11. Alternatively, coincidence arbitration can be achieved by means of joint system design and custom signal processing algorithms[44–46] (cf. Section 3.1).

In order to achieve real-time analysis at high throughput, which is needed for active particle sorting[47,48] or selective enrichment, a high *processing* throughput is also required (*i.e.*, the number of analysed single-particle signals per unit time), thus calling for tailored signal-processing approaches.

2.2 Electrode configurations

Coplanar electrodes. The coplanar electrode configuration consists of patterned electrodes located at the bottom of a microchannel and is used for either absolute or differential measurements. In an absolute measurement scheme, two electrodes are used: voltage is applied to one electrode and the current flowing through the other electrode is collected. The passage of a flowing particle is recorded as a current pulse in each frequency channel. Pulse amplitude and phase are extracted for particle characterization. Absolute measurement schemes are widely used in applications seeking simplicity and portability (*e.g.*, refs. [49–56]). In a differential measurement scheme, three electrodes are used, with voltage applied to the central electrode and the differential current measured at the lateral electrodes (Fig. 2A). Upon the passage of a particle, two current pulses in opposing directions are recorded, which can be modelled as a symmetric bipolar Gaussian shape. In comparison to the absolute measurement scheme, the differential scheme provides higher SNR and the peak-to-peak time can be used to estimate the particle velocity[57]. Differential measurements with three coplanar electrodes are quite common (*e.g.*, refs. [58–64]). Pseudo-differential measurement schemes have also been considered [65]. As an approach to mitigate the number of false positives in absolute measurement schemes, configurations involving multiple coplanar electrodes have been investigated by Javanmard *et al.*[66,67]. Coplanar designs enjoy ease of fabrication, but they are sensitive to the

height of the particle in the microchannel due to the electric field non-uniformity.

Facing electrodes. In the facing electrode configuration, the electrodes are located at the top and the bottom of the microchannel. Compared to the coplanar configuration, this solution creates a more homogeneous electric field distribution (although not completely uniform) and is more sensitive (for identical geometrical parameters) because the electric field is confined into a smaller detection volume[68]. On the other hand, this design requires a more complex fabrication process due to alignment needs. In the most common facing electrode geometry, voltage is applied at two top electrodes and the differential current at the two opposite bottom electrodes is measured (Fig. 2B). As in the three-electrode coplanar design, individual flowing particles generate a signal having a symmetric bipolar Gaussian shape. The differential measurement scheme based on two pairs of facing electrodes, first developed by Gawad *et al.*[12], is used in many research prototypes (*e.g.*, refs.[40,69–71]) and in commercial microfluidic impedance cytometers (*e.g.*, refs.[41,72,73]).

Liquid electrodes. The so-called *liquid electrodes* or recessed electrodes were introduced by Renaud's group[74–76]. The electrodes are positioned at the bottom of dead-end chambers placed on each side of the main channel (Fig. 2C). This configuration creates vertical equipotential surfaces on the apertures of the main-channel walls, if the lateral recess distance of the electrodes to the channel is at least equal to the channel height[76]. Accordingly, the electric field is homogeneous over the channel height, and the chip works as a facing electrode chip rotated by 90 degrees. However, the sensitivity is reduced due to a larger detection length and thus a larger detection volume[77].

2.3 Cytometer designs for increased accuracy

Due to non-homogeneous electric field distribution, nominally identical particles flowing along different trajectories experience different electric field strengths, thereby generating different impedance signals[25,28,57,68]. This introduces blurring of the estimated particle properties, thereby limiting accuracy and reproducibility. To overcome this issue, several approaches have been developed.

Approaches based on mitigation of electric field non-uniformity. A cytometer design based on freestanding 3D electrodes (Fig. 2D) has been proposed by Guiducci *et al.*[78]. It features three vertical electrodes whose faces are aligned to the direction of the flow. This configuration generates a uniform electric field along channel height and allows flexibility in the design of electrode gaps[79].

Approaches based on particle focusing. Focusing systems are used to ensure consistency in particle position. Examples include active focusing systems like acustophoretic focusing[80] and dielectrophoretic focusing[33,81,82], as well as sheath-flow focusing[83]. A sheath flow was used in Song *et al.*[84] to force the particles to move close to a side sensing orifice, thus enabling microorganism detection. Recently, inertial focusing effects in straight rectangular channels[52] or serpentine microchannels[63] have been exploited. Tang *et al.*[85] used inertial focusing in asymmetrically curved channels in combination with a highly conductive feed flow, reaching a detection throughput of 5000 cell/s. Finally, Serhatlioglu *et al.*[61] investigated viscoelastic focusing dynamics in a microfluidic impedance cytometer.

While optimal sample focusing strategies remains elusive, it should be noted[86] that active focusing adds complexity to fabrication; sheath flow systems cause dilution; the high flow rates required for inertial focusing place an inordinate demand on electrical sampling; and viscoelastic focusing is sensitive to rheology of the carrier fluid.

Approaches based on system optimization. Focusing-free impedance cytometry systems based on optimization of the device geometry with respect to the particle of interest have been proposed[86]. They use constriction channels[49,87] or constriction structures that induce self-focusing[88], and are typically limited to a short range of particle sizes. An optimized electrode arrangement involving five pairs of facing electrodes was used in Spencer et al.[89], whereby all non-signal electrode are connected to ground.

Compensation strategies based on electrical metrics of particle position. The inaccuracy introduced in the measured particle properties due to position blurring can be significantly mitigated by means of compensation[90]. To this end, (i) an electrical metric correlating with particle trajectory is identified, (ii) a calibration curve is obtained by using reference particles of known properties, such as size, and (iii) the calibration curve is applied to measured data on particles of interest.

In the typical coplanar electrode chip with the three-electrode differential measurement scheme (Fig. 2A), the pulse width normalized by the peak-to-peak transit time correlates with the vertical position of the particle[58]. By introducing a floating electrode between the stimulating and sensing electrodes (Fig. 2E), a bipolar double-Gaussian signal is obtained, and the relative prominence of the peaks with respect to the saddle in between them, can be correlated with the particle's vertical position[91]. Those metrics were used to achieve accurate sizing of yeasts[58,91] and human blood cells [92,93].

Rewiring the standard facing electrode design by applying voltage and ground to the pairs of diagonally opposite electrodes (Fig. 2F) generates an asymmetric bipolar Gaussian signal due to flowing particles, with the relative difference in peak heights of positive versus negative pulse offering information on vertical position of the particle[94]. This results from the interplay between transverse and longitudinal electric fields established in the sensing zone. Alternatively, by using five pairs of facing electrodes (Fig. 2G), the particle vertical position is encoded by the ratio between transit times relevant to oblique and transverse current paths[90]. The designs in Fig. 2F and G can also be implemented in a liquid electrode configuration, thereby enabling mitigation of measurement sensitivity to particle lateral position.

2.4 Cytometer designs for multiparametric characterization

Typical impedance measurements are focused on the characterization of cell size, membrane capacitance and interior

conductivity, but design solutions that are tailored to enrich the information content of electrical fingerprints have emerged. These designs can be used to provide additional information valuable for monitoring cell position, cell shape and cell mechanical properties, as discussed in this section (see Table 1A and B for an overview)

Electrical position sensing. As discussed in Section 2.3, electrical metrics correlated with particle trajectory have been exploited to increase accuracy of impedance-based cell characterization. From a different perspective, they provide an optics-free and high-throughput way to monitor microscale particle motion at the single cell level. This represents a tremendous opportunity, *e.g.*, to understand fluid motion at the microscale, or to assess the efficiency of microfluidic cell focusing, separation, migration, and sorting. Furthermore, the development of impedance-based position sensors is an opportunity to obtain real-time position feedback for micromanipulation tasks in the field of microrobotics[28].

Wang *et al.*[95] reported a system using a single pair of non-parallel microelectrodes to detect the lateral position of particles flowing in a microchannel on the basis of pulse width (Fig. 3A), however non-uniformity of velocity profile can be a confounding effect. Yang *et al.*[96] presented a system based on N-shaped electrodes (Fig. 3B) that also accounts for particle velocity. Using simple geometric relationships, they derived an analytical expression yielding the particle's lateral position from the measured electrical signal. Particle size characterization was also reported. Solsona *et al.*[97] exploited a gradient in the electric field to detect the particle lateral position (Fig. 3C). Brazey *et al.*[98] presented an impedance based real-time sensor for the detection of the longitudinal particle position (Fig. 3D), which also provided particle velocity. Wang *et al.*[46] predicted the location of particles across ten parallel channels, along with particle velocity and size, by using a code-multiplexed Coulter sensor network (Fig. 3E).

The previous systems were limited to position detection along one axis. The first high-throughput system for electrical detection of cross-sectional (*i.e.*, lateral and vertical) position of individual particles flowing through a rectangular microchannel was presented by Reale at al.[99], combining the design in Fig. 2E (for vertical position detection) with the design in Fig. 2G (in liquid electrode configuration, for lateral position detection). The system was used to investigate inertial particle focusing at different particle Reynolds numbers. More compact design solutions[93,100] (Fig. 3F and G) were subsequently developed and used to monitor hydrodynamic focusing of red blood cells. Impedance-based characterization of cell velocity, size and opacity was simultaneously performed[93].

Designs providing information on cell shape. Besides cell size and dielectric properties, cell shape is a very important feature. As an example, the biconcave shape of the human red blood cell is essential for its biological function, and this feature can be critically affected by genetic or acquired pathological conditions. Cell shape is also a useful indicator when monitoring antibiotic susceptibility of bacteria[101–103] or the budding or fission of yeasts, which are widely used as model systems to study cell cycle progression[82,104–106].

A microfluidic impedance cytometer capable of single cell morphology discrimination under continuous sample flow was presented by Shaker *et al.*[107]. The device, based on liquid electrodes, is fabricated in a cross configuration around a sensing zone (Fig. 4A). This arrangement allows measurement of cell impedance along orthogonal orientations and enables extraction of an index describing cell shape anisotropy. The system was used to monitor shape changes experienced by budding yeasts. A dielectrophoretic focusing and orientation region was introduced before the shape sensing region, to avoid blurring introduced by randomization of particle trajectory and orientation. An impedance cytometer based on particle self-alignment for enabling single-cell morphology discrimination was reported by Xie *et al.*[88]. A constriction structure is introduced to focus the particle stream and a pair of coplanar electrodes are used to record the impedance signal (Fig. 4B). Typical late-budding, early-budding, and unbudded yeast cells were distinguished based on width, amplitude and width-to-amplitude ratio of impedance pulses.

Differential impedance measurements were used by de Wagenaar *et al.*[48] to detect a particular morphological anomaly on the sperm due to presence of cytoplasmic droplets on their flagella. A droplet induced a characteristic bump in the impedance signal and droplet content was quantified by calculating the area under the curve. This area was suitably corrected to mitigate confounding effects due to cell orientation, location and velocity. Zhu *et al.*[108] developed an optimized platform to identify *Caenorhabditis elegans (C. elegans)* developmental stages, eliminating the influence of worm variable morphology.

A microfluidic cytometer for electrical impedance tomography of single flowing cells was proposed by Caselli *et al.*[109]. While progress on this in-silico proof of concept design was limited by fabrication challenges (Fig. 4C), exciting recent developments towards three-dimensional microtubular devices for lab-on-a-chip sensing applications (Fig. 4D) may alter the landscape of microcytometer designs[110,111].

Designs providing information on cell mechanical properties. The mechanical properties of cells have emerged as useful label-free biomarkers for many conditions and diseases[112–114]. Microfluidic single-cell mechanics-based assays typically use expensive imaging systems, making the device bulky and requiring time-consuming post-processing protocols for the massive image data. Exploiting electrical impedance measurements in place of high-speed cameras presents a promising alternative approach. It provides advantages, such as high throughput and simple data processing for enabling rapid and real-time analysis of single cells[115]. Moreover, the combination of mechanical and electrical properties serves as a unique set of intrinsic cellular biomarkers for single-cell analysis, providing better differentiation of cellular phenotypes, which are not easily discerned via just one set of biophysical properties[116]. A few microfluidic impedance cytometers for cell mechanical characterization have been proposed in the last decade (see *e.g.* refs. [113,115] and the references therein). As a common feature, they share a microchannel with constriction regions.

Zhou *et al.*[116] used four pairs of coplanar electrodes to investigate the time required by cells to pass through a constriction (Fig. 4E). The total passage time was divided into two components: the entry time required for a cell to deform and enter a constriction, which is dominated by cell deformability, and the transit time required for the fully deformed cell to travel inside the constriction, which mainly relies on surface interaction of the cell with channel walls. Cells were simultaneously characterized via electrical impedance spectroscopy. Constriction channels separated by relaxation regions have been proposed to improve the discrimination capability, since the relaxation regions provide extra time stamps in the impedance trace. Ren *et al.*[117] designed a chip containing four parallel sensing channels, each one including two constriction regions separated by a relaxation region (Fig. 4F). The ratio of the rise times of the impedance signal magnitude recorded during cell entrance at each of the two constriction regions was used to characterize cell mechanical properties. Bioelectrical parameters were simultaneously collected. A subsequent version of that chip features five sequential constriction channels separated by relaxation regions[118] and was successfully used to distinguish between four different prostate cancer cell lines. Yang *et al.*[115] developed a differential multi-constriction microfluidic device with self-aligned 3D electrodes (Fig. 4G) to simultaneously measure cell deformability, electrical impedance and relaxation index. The total transit time is taken as an indicator of cell deformability. The ratio of the cell transit times through last and first constrictions is used to define an index to quantify the cell relaxation capacity.

2.5 Multizone electrical sensing and other hybrid platforms

Given the versatility of integrating electrical sensing within microfluidic channels, several designs have been proposed, as reviewed below (see Table 1C and D for an overview).

A few reports present systems wherein two (or more) electrical sensing zones are present, typically separated by an intermediate region that is devoted to particle stimulation, manipulation or selective capture. Zi *et al.*[119] investigated cell survival rate by using two electrode pairs separated by a region where cells were exposed to a hypertonic stimulus (Fig. 5A). Reale *et al.*[120] monitored the lateral displacement induced by a dielectrophoretic (DEP) force on cell/particle by electrical sensing in the pre-DEP and a post-DEP zones (Fig. 5B). Caselli *et al.*[44] performed coincidence arbitration of particles flowing in close proximity to each other, by exploiting nonuniformity of particle velocity distribution and comparing the electrical snapshots from two sensing regions that are separated by a hyperbolic constriction (Fig. 5C). Chawla *et al.*[121] proposed a microfluidic analysis unit consisting of two sets of electrodes and a channel of variable geometry to enable counting and size detection of single *Schistosoma mansoni* parasite larvae, and the collective evaluation of the motility of the larvae as an unbiased estimator for their viability. An improved version of that microfluidic unit, featuring simpler operation and higher analysis throughput, has been recently reported[122].

Leveraging on the idea of antigen-based electrical labelling[123,124], Valera *et al.*[59] presented a platform to detect proteins in undiluted human plasma samples. The device uses a differential enumeration platform that integrates two electrical counting zones, antigen specific capture chambers, and bead-based immunodetection to quantify cytokines. Similarly, Liu *et al.*[125] used multiple electrical sensors for cell immunophenotyping against multiple antigens. The microfluidic device (Fig. 5D) consists of an array of microfluidic cell capture chambers, each functionalized with a different antibody to recognize a target antigen, and a network of code-multiplexed Coulter counters placed at strategic nodes across the device to quantify the fraction of cell population captured in each microfluidic chamber.

Other works used electrical impedance sensing of flowing cells in combination with other sensing modalities, like high-speed imaging of flowing cells[126] or of cells invading into side constriction channels[127] (Fig. 5E), time-lapse microscopy of growing cells[128] (Fig. 5F), or impedance spectroscopy of trapped cells[129] (Fig. 5G).

Platforms combining impedance sensing with dielectrophoretic manipulation[130], or with inertial microfluidics for sample enrichment[52] or sample fractionation[63], have also been recently developed. Farmehini *et al.*[130] used the voltage drops determined from impedance measurements to compute the fraction of applied voltage used for contactless dielectrophoretic particle manipulation at each frequency of interest. In this manner, they envisioned the integration of impedance measurements on the dielectrophoresis chip to account for chip-to-chip variability due to microfabrication errors. Raillon *et al.*[52] developed a label-free high-throughput platform to isolate, enumerate, and size circulating tumour cells (CTCs) on two coupled microfluidic devices (Fig. 5H). Cancer cells were purified through a Vortex chip (Vortex Biosciences) and subsequently introduced in-line to an impedance chip, where a pair of electrodes measured fluctuations of an applied electric field generated by the passing cells. Petchakup *et al.*[63] presented a multi-staged platform that enables isolation of neutrophils and monocytes from diluted or lysed blood samples directly within minutes, based on Dean Flow Fractionation (DFF) (Fig. 5I). DFF-purified leukocytes are inertially focused in serpentine channels into single stream prior to impedance detection.

Feng *et al.*[131] combined impedance cytometry and droplet microfluidics to monitor the osteogenic differentiation of single bone marrow mesenchymal stem cells in droplets. The device enabled single-cell trapping, positioning, and impedance measurements of individual cells.

It is noticed that many platforms (*e.g.*, refs.[121,128,131,132] also allow for parallelization of the analysis units, resulting in increased throughput.

2.6 Portable platforms

One of the current challenges in the development and commercialization of lab-on-a-chip microsystems is the integration and miniaturization of all the components that are

required for chip operation at the point of care facility, spanning from sample preparation to detection[133,134]. To this aim, integrated impedance-based devices have been recently developed. Credit-card-sized cell counters have been implemented, based on modular microfluidics[65] or based on a CMOS lock-in application-specific integrated circuit, combined with an event counter that is embedded in a field-programmable gate array[133]. Smartphone-based cytometers are also being developed, where the smartphones function to replace benchtop computers or laptops for the purpose of receiving and analysing the collected data[135]. Furniturewalla *et al.*[51] presented a wearable microfluidic impedance cytometer implemented on a flexible circuit wristband with on-line smartphone readout. Moreover, in order to reduce the costs related to electrode microfabrication, devices with integrated micro-needles[136], devices with integrated Field's metal microelectrodes[137], and PCB-based solutions have been proposed[138]. Finally, the use of electronically barcoded particles[50,56,139] is being explored as a tool for point-of-care diagnostic applications.

3 Data analytics

In this section, we review the tools for data analytics that are used in microfluidic impedance cytometry. First, we discuss the signal-processing strategies adopted to extract single-cell features from the raw impedance signals (Section 3.1). Then we present an overview of the available modelling approaches (Section 3.2), which are used for the interpretation of the device response and for in silico design, or to correlate raw impedance features to biophysical cell properties (Section 3.3). Finally, we review population-level data analysis that enables cell phenotyping (Section 3.4).

3.1 Signal-processing of raw data streams

The analysis of raw signals for parameter extraction to enable recognition of phenotypes at the single-cell level requires sturdy signal processing. Herein we provide a description of the signal processing techniques that may be implemented to extract the information embedded in the raw impedance signals. Even though the particular chosen approach may depend on the specific system design utilized, the following steps can be generally identified: signal conditioning, segmentation, feature extraction, and feature processing, which are discussed below. A typical workflow is presented in Box 1.

Signal conditioning. Recorded data streams (*i.e.*, demodulated electrical currents) typically exhibit some noise and baseline drift. In order to improve signal quality, denoising and detrending are usually performed. Classical signal processing tools may be implemented, such as moving-average filter[98], Savitsky–Golay filter[33], or wavelet-based denoising[119].

Segmentation. This refers to the identification of data stream portions corresponding to cell passage in the sensing region. When multiple channels are acquired from the same sensing zone, the channel(s) with the best SNR is/are preferably used for segmentation, in order to increase sensitivity and robustness towards detection of artefacts.

Segmentation is usually performed by means of thresholding and peak-finding. This can be done on the conditioned signal (*e.g.*, refs. [48,65]), in the wavelet-domain[33], or after correlation with a suitable template (*e.g.*, refs.[29,140]). Derivative-based approaches have also been implemented to detect local maxima (*e.g.*, ref.[86]).

An alternative approach is the identification of idle time frames (*i.e.*, data stream portions not containing events). As an example, Liu *et al.*[141] used the zero crossing rate (ZCR) as the discrimination parameter, since ZCR of the noise is greater than that of signal recorded during cell passage.

Feature extraction. As shown in Box 1, the features to be extracted (from each frequency channel) are often peak-amplitudes and peak-to-peak transit times. The feature extraction may be a direct outcome of the segmentation, especially when the latter is based on peak-finding. However, peak-finding may provide inaccurate results if residual noise is present in the data stream.

In order to achieve robust feature extraction, or when the electrical fingerprints have peculiar shapes, approaches based on correlation with design-tailored templates can be used[29,91,94,142]. As an example, a bipolar Gaussian template can be used for the differential current in case of classic designs[29] (Fig. 1A and B). Moreover, inter-channel correlations can be exploited. As an example, although the peak amplitude varies significantly among the different frequency channels and between the real and imaginary signal parts, the peak-width and the peak-to-peak time of the measured signals are quite similar. Accordingly, a unique bipolar Gaussian template characterized by a complex frequency-dependent amplitude may be used to process all frequency channels at the same time[64]. Generally, template-fitting strategies have higher computational cost than peak-finding strategies. An emerging alternative that potentially enables both, accuracy and real-time processing, is given by neural network-based approaches (cf. also Table S2 of the Supplementary Material). By using a recurrent neural network, Honrado *et al.*[100] showed the characterization of red blood cells and yeasts with a unitary prediction time of 0.4 ms. Wang *et al.*[46] trained a convolutional neural network to analyse waveforms from a network of ten code-multiplexed Coulter counters (Fig. 3E) at high processing speed. Their network was also capable of resolving interferences generated by coinciding particles.

In fact, multiple particles may reach the sensing zone in close proximity, generating a plethora of possible signal shapes from which single particle features cannot be reliably extracted, unless joint system design and custom signal processing algorithms are implemented. Kellman *et al.*[45] presented a method to perform individual particle coincidence correction in a Coulter counter, inspired by multiple-user communication theory. They modulated the channel response, introducing wider and narrower regions to give each particle a binary Barker sequence signature, and applied a successive interference cancellation method to separate coinciding particles. Caselli *et al.*[44] proposed a model of the signals generated by coinciding

particles in a microchannel comprising two electrical sensing zones (Fig. 5C) and used maximum a posteriori probability estimation to characterize individual particle properties, thus enabling accurate RBC counting at 2500 cell/s. In a following work[143], in order to reduce the computational time, a machine-learning based approach was developed (cf. Table S2).

Besides coinciding particles, other application-specific or design-specific situations may give rise to peculiar signal shapes that call for tailored signal processing algorithms. Zhu *et al.*[108] measured *C. elegans* worms and employed Gaussian kernel density estimation to efficiently extract the baseline-to-plateau current magnitude, in presence of drastic spikes generated by motion of the worms. Zhang *et al.*[87] used kernel density estimation and binarization to identify the time duration of three subsequent pulses generated in the signal waveform as the cell passed through an asymmetric constriction channel (cf. Fig. S2). Brazey *et al.*[98] used an extended Kalman filter for real-time detection in a noisy environment. Saateh *et al.*[62] developed a user-friendly software for real-time impedimetric droplet measurement.

Feature processing. Before being used for population-level data analysis (Section 3.4), the single-cell features extracted from each frequency channel, such as complex peak-amplitude, pulse width, peak-to-peak times, etc., may undergo further processing to mitigate measurement errors (*e.g.*, compensation for position blurring or for flow fluctuations). Moreover, by means of suitable models it is possible to correlate the raw impedance features to cell biophysical parameters (Section 3.3).

3.2 Modelling approaches for microfluidic impedance cytometry

Foundational analytical and numerical modelling approaches for microfluidic impedance cytometry were described in Gawad *et al.*[12] and Sun *et al.*[144]. They include equivalent circuit models (ECM), Maxwell's mixture theory (MMT), and finite element method (FEM). While we refer the reader to the previous literature for an extensive presentation of the relevant theory, we provide a synthetic view of those approaches in Box 2 (cf. also Section S1 and Table S1 of the Supplementary Material).

Equivalent circuit models and Maxwell's mixture theory. Equivalent circuit models describe the device in terms of a combination of lumped circuit parameters and are widely used to understand the frequency response of the system (*e.g.*, refs.[53,54,87,131,145,146]). As an example, in Box 2A(i) we report an equivalent circuit model of the standard facing electrode design in a differential measurement scheme[12]. The electrical impedances associated with stray capacitances (Z_{st}), electrical double-layer (Z_{dl}), medium-filled channel (Z_{med}) and channel with a suspended cell (Z_{mix}) are shown. By using a simplified model[13,147] (Box 2A(ii)), the impedance Z_{mix} is described as the parallel of medium capacitance (C_{med}), medium resistance (R_{med}), and the series of membrane capacitance (C_{mem}) and intracellular resistance (R_{int}).

As shown in Box 2A(iii) the impedance Z_{mix} can be directly related to the geometric and dielectric properties of the system by using Maxwell's mixture theory (cf. *e.g.* Sun et al.[144]). Under the assumption of small volume fraction φ (defined as the volume ratio of the cell to the detection area), the complex permittivity of the cell-medium mixture ($\tilde{\varepsilon}_{mix}$) is given in terms of the complex permittivity of the medium ($\tilde{\varepsilon}_{med}$), the volume fraction, and the complex Clausius-Mossotti factor ($\tilde{f}_{CM}$). The latter accounts for the complex permittivity of the cell ($\tilde{\varepsilon}_{cell}$) that is generally computed by using suitable shell models[14,15]. As an example, we report a single-shell spherical model (Box 2A(iv)) assuming that the cell membrane thickness (d_{mem}) is much smaller than the cell radius (r). Since Maxwell's mixture theory assumes uniform field, a geometric correction factor G has to be included in Z_{mix} to account for fringing fields[12,68].

By using MMT and neglecting stray capacitances, the following approximate expression for the differential current is obtained (Box 2A(i)):

$$I_{diff} \cong -\frac{V_{appl}}{Z_{med}}\frac{1}{[1+(2Z_{dl}/Z_{med})]^2}3\varphi\tilde{f}_{CM} \qquad (1)$$

where V_{appl} denotes the applied potential, cell volume is embedded within φ, and cell dielectric properties are embedded within $\tilde{f}_{CM}$. The sensitivity of the differential current I_{diff} to cell properties ($\varphi\tilde{f}_{CM}$) depends on the current flowing in the empty cytometer (V_{appl}/Z_{med}). At low frequency, the double-layer impedance Z_{dl} may significantly reduce this sensitivity. The current I_{diff} multiplied by the transfer function of the acquisition system ($H(\omega)$) provides the amplitude of the measured signal S. Therefore, S also depends on frequency-dependent phase and gain of the acquisition system.

Finite element method. In comparison to ECM and MMT, finite element methods are computationally more demanding, but can account for the geometric and electric details of the system and of the flowing cell, thereby removing some simplifying assumptions. For instance, cells with arbitrary volume, shape, orientation and position in the channel can be simulated, and the electric field non-uniformity is automatically accounted, without the need for correction factors. The specific dielectric properties of each subcellular feature (*e.g.*, cell membrane, cytoplasm, and nucleus) can be easily accounted, by assigning appropriate parameter values to the various geometric subdomains of the model. Furthermore, by using finite elements, the whole signal waveform recorded as a cell passes through the sensing region of the device can be simulated. Experimental details, such as distribution of particle sizes, dielectric properties, inter-arrival times, velocities, and trajectories can be accounted, along with an allowance for the measurement noise. Hence, a *virtual laboratory* can be developed using finite-element-based approaches, providing synthetic data streams that closely mimic experimental conditions[148,149]. As such, finite element simulations are widely used for in silico device design, testing and optimization, thus allowing a reduction of time and resources needed to move from novel ideas to prototypes[62,77,86,93,97–99,108,150]. Moreover, synthetic data streams obtained via finite elements are a valuable resource to assess the performance of the signal processing routines used to process the measured impedance signals. While optical methods could be used as the gold

standard, they require suited equipment and image-processing algorithms, and they may have a certain level of uncertainty (*e.g.* due to limited resolution or algorithm-induced errors). Since biophysical properties of virtual particles passing through the system are known based on the synthetic impedance signal streams, performance metrics (*e.g.*, sensitivity, positive predictive value, errors in estimated particle properties) of signal processing algorithms can be quantified[46,100,140]. Similarly, synthetic data streams could be used to investigate the extrapolation capability of neural networks designed for recognitions of cell phenotypes.

As summarized in Box 2B, FEM model equations include the conservation of the electric current density $\boldsymbol{J}$ in the intracellular space and in the suspending medium, the insulating boundary condition over the channel walls, and the equation accounting for the electrode double-layer capacitance. To optimize mesh quality, the cell membrane is preferably modelled as an interface with a contact impedance between the intracellular space and the medium, rather than a very thin three-dimensional domain. Accordingly, the electric current flux is continuous across the interface, whereas the electric potential is discontinuous, with a jump depending on membrane conductance and capacitance per unit surface, σ_{mem}/d_{mem} and $\varepsilon_{mem}/d_{mem}$, respectively. Any geometric structure with small thickness-to-surface ratio is better modelled as an interface, as shown for cell membrane. The model can be easily modified to account for additional features, like for instance the presence of cell nucleus or cell wall[82]. For prescribed applied potentials over the electrodes, the distribution of the electric potential V in the device is solved and the electric currents through the electrodes are computed by integration.

In order to find an optimal compromise between computational cost and solution accuracy, the mesh should be wisely designed. In particular, it should be finer near the electrodes and around the cell membrane, wherein higher field gradients are expected, and coarser elsewhere.

Simulating the signal produced by a flowing particle requires a series of FEM analyses, involving different meshes for different particle locations. Unfortunately, rather noisy simulated signals are generally obtained due to mesh variations, unless extremely fine meshes are used. As a matter of fact, smooth, accurate signals can be obtained, using even relatively coarse meshes, as long as two sets of FEM analyses with the same mesh are performed for each particle location, one with the particle inside the measuring zone and another one with the particle replaced by the suspending medium. By subtracting the results of the two simulations, the mesh-generated numerical noise can be effectively cancelled out.

Moreover, sometimes it can be convenient to model the device as a network of admittances. The admittance matrix of the network (depending on cell properties and location) is computed by performing a suitable single set of finite element analyses[109]. Based on this, different wiring schemes can be readily modelled, solved and compared.

3.3 Cell biophysical characterization by model fitting

Equivalent circuit models, Maxwell's mixture theory, and shell-models have been widely used to compute cell dielectric properties by fitting simulated impedance spectra to measured ones (*e.g.* refs.[69,89]). To this aim, the signal associated with each cell (S^{cell}) is usually normalized with respect to the signal measured using reference beads (S^{bead}), to cancel the transfer function of the acquisition system. In particular, normalization enables comparison of cells based on their impedance frequency response, since field penetration through the reference bead is invariant versus frequency. In order to differentiate cells from beads, a reference high frequency channel (*e.g.*, 18 MHz) is typically used, wherein there is no field penetration through beads (*e.g.*, ref.[151]). Assuming the experimental setup described in Box 2, the normalization is computed as follows[89]:

$$\frac{S^{cell}}{S^{bead}} = \frac{\tilde{f}_{CM}^{cell}\varphi^{cell}}{\tilde{f}_{CM}^{bead}\varphi^{bead}} = \frac{\tilde{f}_{CM}^{cell}}{\tilde{f}_{CM}^{bead}}\left(\frac{r^{cell}}{r^{bead}}\right)^3 \qquad (2)$$

where the superscripts refer to cell or bead parameters. Accordingly, the unknown dielectric properties of the cell ($\tilde{f}_{CM}^{cell}$), along with its size can be found by multiplying the experimentally measured quantity (S^{cell}/S^{bead}) by a calibration factor ($\tilde{f}_{CM}^{bead}$):

$$\tilde{f}_{CM}^{cell}\left(\frac{r^{cell}}{r^{bead}}\right)^3 = \tilde{f}_{CM}^{bead}\frac{S^{cell}}{S^{bead}} \qquad (3)$$

By fitting a suitable shell model to the above (calibrated) data, measured based on several frequencies, the dielectric properties of the subcellular features that appear in the expression of $\tilde{f}_{CM}^{cell}$ can be estimated – refer to Section S1 of the Supplementary Material for further details. As an example, in case of a single-shell model, it is possible to estimate (cf. Box 2): permittivity and conductivity of the intracellular space (ε_{int} and σ_{int}, respectively) and membrane capacitance ($\varepsilon_{mem}/d_{mem}$), while membrane conductance (σ_{mem}/d_{mem}) is typically neglected. By using multi-shell models additional parameters can be estimated, such as conductivity and permittivity of the cell wall, as in case of yeasts or bacteria[152,153], or the dielectric properties of intraerythrocytic parasites[69]. The inclusion of multiple shells, however, comes at the cost of model complexity, processing time and overall confidence in the fitted data. By increasing the number of modelled shells, more parameters must then be considered and iterated, resulting in longer modelling/fitting times. Furthermore, initial values and boundaries for each modelled parameter need to be defined, with the risk of biasing the modelling outcome. Commonly accepted values from previous literature are often used. This not only permits certain parameters to be fixed at a specific reference value but also allows for other parameters to be further varied and/or to include additional shells, without compromising complexity and processing time.

Typically, the mean dielectric properties of a homogeneous population of cells are determined[69,71]. As an example, experimentally measured impedance spectra of malaria parasite infected-RBCs[69] are shown in Fig. S1A, along with their

best fit (double-shell oblate spheroid model). In that figure, each data point is the average impedance over at least 150 cells. In Spencer *et al.*[89], the impedance spectra of single flowing RBC ghosts were reported (Fig. S1B). The latter were obtained by simultaneously applying eight frequencies to the stimulation electrodes. Accordingly, the electrical properties of thousands of single cells at high throughput were determined.

Although fitting of impedance spectra generally requires measurements at several frequencies, Chen's group[87,127,154] developed a high-throughput approach to quantify single-cell intrinsic bioelectrical markers by simultaneous application of just two frequencies. In a recent work[87], they introduced a microfluidic platform composed of an asymmetrical constriction channel through which single-cells are forced to squeeze, while capturing impedance profiles (amplitude and phase waveforms) (Fig. S2). A number of features are extracted from the raw impedance signals and then translated into values of specific membrane capacitance, cytoplasm conductivity and cell diameter, by using an equivalent circuit model and channel geometrical parameters. Mahesh et al.[155] proposed an approach to estimate cell size and cell membrane capacitance with a single frequency, by exploiting a fine feature of the reactive current.

While modelling approaches to obtain cell dielectric properties are well-established and widely used, models capable of translating impedance-based measurements (*e.g.*, cell transit time through a constriction channel) into biomechanical cell properties are in their infancy. This is mainly due to the complexity of the cell deformation process, including: non-linear mechanical constitutive behaviour, large deformations, contact and friction, fluid-structure interactions. These features require complex, computationally-demanding numerical integration schemes. Accordingly, phenomenological parameters (*e.g.*, relaxation indices computed as transit time ratios), rather than biophysical parameters, are generally used in impedance-based deformability cytometry. Simple viscoelastic cell-models were used to characterize the instantaneous Young modulus[156] or the cytoplasmic viscosity[127] of cells in a microfluidic impedance chip, wherein optical measurements of cell aspiration length, rather than electrical metrics, were used as input for the analysis. There is a need for tailored device designs and coupled modelling approaches to bring impedance-based deformability cytometry to its full maturity.

3.4 Cell population data analysis: clustering into phenotypes

Investigations on a multitude of sample types using impedance cytometry have been performed in recent literature (see Section 4 for an in-depth exploration of recently published work). The analysis of impedance cytometry data invariably relies on the visualization of data in terms of specific features (*e.g.* impedance magnitude and phase, transit-time) represented as scatter-plots, histograms, frequency relaxation spectra or other methods to discern clusters of specific phenotype(s) present in the data. Box 3 provides a broad suggestive guideline on how to perform data visualization and analysis.

An examination of published material shows that a common practice in cell population data analysis is to acquire impedance data using low frequencies (≤ 1 MHz). Impedance data at low frequencies allows for inferences on cell size to be drawn, either based purely on signal magnitude or on estimated electrical diameter (using reference particles). Differences in cell size are the most frequently used biophysical parameters to distinguish cell types and even perform separation[157–159]. Thus, when performing impedance cytometry measurements of heterogeneous populations, it is valuable to gather data at the low frequency range, so that subpopulations of varying size can be distinguished and properly gated (*e.g.* RBCs *versus* WBCs *versus* cancer cells).

Signals from multiple frequencies are also commonplace in recent literature, since specific frequency ranges supply information about different cell properties (Fig. 1). Thus, impedance data in the form of magnitude (sometimes referred to as amplitude) and phase at different frequencies are regularly used to plot and analyse data. Moreover, these different variables can also be used to calculate metrics that further probe cell properties and can give qualitative estimations of certain dielectric properties, with the best known example being magnitude opacity[40,55,57,60,63,71,160,161]. Being the result of the ratio of impedance magnitude at mid-range frequency (*i.e.*, 1–10 MHz) over impedance magnitude at low frequency (*i.e.*, 0.1–1 MHz), this metric effectively probes membrane properties and is inversely related to membrane capacitance[36,160]. It has been widely used in recent literature to profile different cell types[40,60,63,71] or assess alterations to membrane properties due to different interventions[55,161].

Quantitative electrophysiological cell properties derived from dielectric modelling can also be used to plot and analyse cell populations (as explored in Section 3.3). However, only recently have these models been able to do so at a single-cell level[89,154,156,162,163], thereby making these properties (*e.g.* C_{mem} or σ_{cyt}) available as another component of the overall data analysis process, while unveiling the presence of subpopulations and different phenotypes in the analysed samples.

Contingent on the homogeneity/heterogeneity of samples, the clustering of data and gating process can be rather involved, with different approaches being available. The simplest method relies on "manually" gating clusters of data that are evident on the data plot. This approach is easily implementable and probably satisfactory to many sample types. However, by its nature, this method can be unreliable and skew the perception of the data, as it often depends on familiarity with the subpopulations expected to be found in the data. Other methods rely on the fitting of normal distributions to the data, be it 1-dimensional Gaussian fits to histograms or 2-dimensional Gaussian fits to scatter plots, for example. By identifying normal distributions in the data, gates can be generated to cluster the data into subpopulations. However, such approaches are not easily implemented (specially for 2D distributions) and rely on

the presence of normally distributed populations, which need not be the case for all sample types.

Another analysis method that has gathered much interest in recent literature focuses on machine learning-based classification of different cell subpopulations (cf. also Table S2 of the Supplementary Material). In particular, support vector machines[53] and neural networks[115,154] have been used as supervised classifiers based on impedance cytometry data. These methods allow for a quasi-real-time analysis of data, limiting human interference into the gating strategy, but these need to be trained with a representative dataset.

4 Phenotyping cell populations

The juxtaposition of single-cell versus large population-level analysis has presented itself as a recurrent topic of debate within the microfluidics community at large[164], and is the manifestation of a crucial question regarding any cell population analysis: how homogeneous can a given sample be? Bulk analysis techniques are generally simple to use and readily available (*e.g.*, PCR or Raman spectroscopy), however, cells exposed to seemingly identical environmental stimuli will often display a distribution of heterogeneous behaviours. A collective averaging of results could thus cause the loss of crucial information regarding the population makeup, potentially giving rise to misleading results. In contrast, high throughput single-cell analysis offers the capability to, not only analyse large quantities of individual cells, but also to identify the distribution of responses, along with measuring statistically relevant numbers to make inferences from the data. Consequently, it is advantageous for the analysis of impedance cytometry data to be performed at a single-cell population level, be it in the form of electrical features (*e.g.* impedance phase or magnitude) or extracted biophysical parameters (*e.g.* electrical size or dielectric properties), so that the single-cell data can be analysed for the presence of various subpopulations in the heterogeneous sample. It is by this process that different phenotypes can be identified for cells under specific external stimuli (*e.g.* modifications during differentiation, stages of infection, activation processes, or differences in drug resistance or therapeutic potential, to name a few examples).

Table 2 offers an extensive list of literature focused on cell population analysis. Recent literature has focused on investigating a wide variety of cell types to identify and characterize specific phenotype(s) present in the samples of interest. The following section will focus on highlighting some of those approaches. Table 3, found at the end of this section, presents a broader view on the key phenotypical findings. With the interest in studying cell samples originating from tumour xenografts or model cancer cell lines increasing in the recent years, we divide the scope of the work performed with cancer cells into three independent sub-sections. These sub-sections cover the studies probing the role of electrophysiological phenotypes to understand disease presentation and single-cell dielectric properties (Section 4.1); biomechanical phenotyping studies (Section 4.2); and the application of electrophysiological phenotypes as a metric to assess cell viability and drug sensitivity (Section 4.3). The remainder of this section covers the works focused on a variety of sample types: mammalian cells (Section 4.4), human pathogens (Section 4.5), yeast cells (Section 4.6) and others (Section 4.7).

4.1 Cancer cells – Phenotypical characterization

The majority of recently published literature utilize cancer cell lines, either from long-standing established model cell lines or from patient derived xenografts, with a focus on phenotypical characterization of various cancer cell types. The Chen Group[87,127,154,156,162,163,165] used a narrow microfluidic constriction channel (*e.g.*, Fig. 5E and Fig. S2) for extraction of single-cell specific dielectric properties using equivalent circuit models (Sections 3.2 and 3.3). It is noteworthy that this squeezed state of the cell may alter the measured electrical activity due to its effects on the cell membrane[166]. This system was applied to the phenotypical characterization of CTCs from hepatic, oral and lung and the identification of EpCAM+ CTCs after their isolation[162]. (Fig. 6A). For hepatic and oral cancer samples, EpCAM+ CTCs had an estimated lower C_{mem} and higher σ_{cyt} than EpCAM- CTCs. Furthermore, significant differences in C_{mem} and σ_{cyt} were observed between the studied cancer cell types. In an updated system[154], microchannels defining a crossing constriction were capable of measuring >100 cells/s, allowing acquisition of >100,000 cells per sample type analysed. To evaluate the updated system, H1299 and HeLa model cell lines were compared, with significant differences in C_{mem} and σ_{cyt} being observed between these cells (Fig. 6B). A neural network-based pattern recognition tool was used to classify cell types based on their estimated dielectric properties (cf. Table S2), with classification success rates above 90% and 75% for the distinctions of H1299 versus HeLa cell lines and A549 versus EMT-activated A549, respectively.

A follow-up work[163] presented the capability of distinguishing between adenoid carcinoma cell line SACC-83 and lung metastasis cell line SACC-LM, with metastatic cells presenting a lower C_{mem} and higher σ_{cyt}. Liang *et al.* followed with the characterization of the dielectric properties of single-nuclei from cancer cell lines A549 and SW620[165]. By varying the constriction device to allow for trapping of individual isolated nucleus, the extracted dielectric properties (nuclear envelope capacitance (C_{ne}) and resistance (R_{ne}) and nucleoplasm resistance (R_{np})) were used to show significant differences in R_{ne}, between the tested cell types. In another approach[129] based on integration of hydrodynamic constrictions to passively trap single cancer model cells (HeLa, HepG2 and A549), temporal analysis of cells was possible using electrical impedance spectroscopy (EIS), where significant differences were observed between cell lines for impedance magnitude data at 1MHz (Fig. 6C); while non-trapped flowing cells were analysed by standard impedance flow cytometry (IFC) (Fig. 5G). Such strategy, combining both IFC and EIS in a single system, could thus yield more data-rich results, improving the phenotypical characterization.

More recently, McGrath *et al.*[71] presented a comprehensive study aiming at the phenotypical stratification of patient-derived, pancreatic tumour xenografts based on their tumourigenicity. Using a high-throughput system (>300 cells/s), single cells derived from primary pancreatic tumours versus those from liver metastasis were analysed with a novel impedance phase contrast metric, which is based on impedance phase variations in the high and low frequency range. Variations in this metric were found to be related to electrophysiology of the cell interior and to be systematically altered as a function of tumourigenicity (Fig. 6D). Moreover, dielectrophoresis was performed in parallel and confirmed that cancer cells of higher tumourigenicity exhibited lowered interior conductivity and enhanced permittivity. Genetic analysis also confirmed that dysregulation of Na^+ transport and Ca^{2+} removal from the cytoplasm is present in more tumourigenic cell lines, further validating the phenotypical characterization.

4.2 Cancer cells – Biomechanical phenotyping

Another topic of emerging research interest in recent literature is the integration of methods to determine biomechanical phenotypes of cells based on impedance cytometry. The measurement of mechanical and electrical properties of single cells can yield useful information on the physiological and pathological state of cells. Based on the constriction channel device, the Chen Group[156], estimated the dielectric (C_{mem} and σ_{cyt}) and mechanical properties of single-cells from model cell lines (H460, H446, A549, 95D and 95C), with the latter measured through instantaneous estimation of Young's modulus (E_{inst}) using a numerical mechanical model applied to high-speed camera images. (Fig. 6E).

In another constriction-based system (Fig. 4E), four pairs of electrodes were included for the acquisition of impedance magnitude data and different time metrics (*i.e.* entry, transit and passage times) of individual cells, to characterize the deformability of MCF-7 model cells[116]. The system was used to characterize the deformability and impedance phenotypes of normal, fixed and (phorbol 12-myristate 13-acetate) PMA-modified MCF-7 cells, while RBCs were used as highly deformable reference particles. Alterations to cell deformability by fixation (decrease) and PMA modification (increase) were confirmed based on time metrics and presented together with differences in impedance magnitude (Fig. 6F).

A system comprised of multiple constriction regions was presented by Yang *et al.* to characterize the biophysical phenotypes of model MCF-7 cells[115]. Using 3D electrodes, impedance and deformability measurements of single cells based on the transit-time through the constrictions (Fig. 4G) were used to distinguish biophysical properties of untreated, nethylmaleimide-treated and cytochalasin B-treated MCF-7 cells. A back propagation neural network (cf. Table S2) yielded a classification accuracy of more than 90%, when impedance and deformability metrics were considered together, demonstrating its applicability to the analysis of concurrent biophysical and impedimetric data.

4.3 Cancer cells – Viability assessment

Another area of interest when studying various cancer cells is the determination of cell viability and the phenotypic alterations observed due to loss of viability by apoptosis or necrosis, specifically under chemotherapeutic drug treatments. Xie *et al.* proposed non-traditional parameters based on admittance (*i.e.* the reciprocal of impedance) as new metrics to discriminate live, necrotic and apoptotic cells[49]. Specifically, conductance (G, the real part of admittance) and susceptance (B, the imaginary part of admittance) were used. Proof-of-concept demonstration was performed using HeLa and Jurkat cells treated with an apoptosis-inducing drug Actinomycin D (AD). Higher concentrations of AD represented smaller G and B. Comparison between the phenotyping of cells using the novel G and B metrics versus standard flow cytometry was performed, with the ratios for viable, early apoptotic and necrotic/non-viable cells showing good correlation.

De Ninno *et al.*[64] presented a three-electrode coplanar device capable of discrimination between live, necrotic and apoptotic cells at high-throughput (~200 cells/s). Cells from lymphoma model cell line U937 were either treated with etoposide (an apoptosis-inducing drug) or subjected to a heat-shock (to induce a loss of viability and mimic natural necrosis). Results suggest that using electrical diameter (estimated using 500 kHz impedance magnitude) it was possible to discriminate between intact cells and smaller cell debris (possibly apoptotic bodies and/or necrotic cell fragments; Fig. 6G). Within the cell population, viable and necrotic cells were discriminated based on clear differences in impedance phase data at 500 kHz. Impedance phase at 10 MHz was used to identify two subpopulations of cell debris of differing phenotype, possibly due to capacitance and conductivity differences between apoptotic bodies and other cell fragments present.

In another work using the same lymphoma cell line[41], the viability of cells was found to be compromised by exposure to toxic nanomaterials (NMs) at various concentrations and time-points. After optimization steps for the acquisition conditions (*e.g.* frequency and buffer composition), a clear discrimination between viable and necrotic cells was obtained at 6 MHz using a buffer comprised of PBS to 0.28M sucrose solution at a 1:4 ratio (Fig. 6H). In fact, the effect of NMs on cell viability could not be assessed using trypan blue dye exclusion and flow cytometry, due to interference of NMs on the staining process using Annexin-V/7-AAD. This highlights the utility of impedance-based viability assessment systems for cases wherein labelling cannot identify functional alterations.

Supervised machine learning was implemented to perform viability assessment of drug-treated cancer cells (model T47D cell line) in a different approach[53]. Since activated matriptase (a membrane-bound protease), is overexpressed in various epithelial cancers, cells were subject to an anti-matriptase-conjugated drug, inducing apoptosis and loss of viability. Cells sensitive to the drug presented changes in impedance magnitude and phase data with respect to drug insensitive cells (in the 500 kHz - 30 MHz range). Support vector machines, using an 8-feature matrix (impedance magnitude and phase at 4

different frequencies), had an overall accuracy of > 95% in predicting the viability of analysed cells (cf. Table S2). These results highlight the value in implementing machine learning protocols (such as neural networks) to streamline cell viability assessment, without the need for staining or labelling.

4.4 Mammalian Cells

Considering other mammalian cells, studies on various leukocytes populations in human blood has been a major focus. These cells play important roles in immune response, infections, cancer and other diseases. However, immune systems can become compromised as a consequence of certain diseases, with an example being diabetes, wherein key metabolic pathways are altered, thereby dysregulating many components of both the innate and adaptive immune systems. This effect was studied by Mahesh *et al.* using a system for biomechanical and electrical phenotyping of lymphocytes from diabetic patients[145]. The device was comprised of a constriction channel wherein alterations to the mechanical properties of single cells was estimated based on differences in the transit-time of cells through the narrowing region, with pairs of electrodes at the entrance and exit of the constriction measuring single-cell signals. Results showed a significant increase in the transit-times of diabetic versus normal lymphocytes, indicating a loss of deformability by lymphocytes from diabetic patients (Fig. 7A). Significantly higher signal amplitude differences were also observed for the altered lymphocytes, indicating overall changes to the electrophysiology of diabetic lymphocytes, likely connected to alterations in the cytoskeleton of cells.

Another work focused on the profiling of diabetic leukocytes was proposed by Petchakup *et al.*[60]. An innovation presented in this work was the utilization of a microfluidic device to perform a size-based, inertial cell sorting step (using Dean flow fractionation - DFF) to enrich for specific leukocyte populations prior to impedance cytometry (Fig. 5I). DFF-sorted leukocytes populations of monocytes, lymphocytes and neutrophils were clearly distinguishable from other blood cells on the basis of their impedance magnitude and magnitude opacity phenotypes (Fig. 7B). The activation of DFF-sorted monocytes with inflammatory stimulus from TNF-α induced alterations to the membrane as apparent by an increase in magnitude opacity, while LPS stimulation was used to pick out two subpopulations: activated monocytes and non-activated neutrophils within the expected homogeneous sample. Considering DFF-sorted samples from diabetic patients, the phenotypes of neutrophils presented significantly higher magnitude opacity versus that of monocytes, suggesting that diabetic patients would likely have neutrophils/monocytes expressing pro-inflammatory/activated phenotype, which can possibly serve as a novel biomarker for the inflammatory response.

In a follow-up work, impedance cytometry detection was integrated within the DFF sorting device[63]. Focusing again on diabetes, the capability of healthy and glucose-treated neutrophils to form neutrophil extracellular traps (NETosis, an anti-inflammatory defense function, wherein web-like DNA structures are used to trap and kill pathogens) was assessed. Cells undergoing calcium ionophore (CaI) induced NETosis were measured, with NETosis neutrophils presenting a higher magnitude opacity and cell size than unstimulated neutrophils, especially at 120 min (Fig. 7C). These alterations could be related to cell membrane and cytoplasm conductivity alterations, together with the alteration of internal structure and degradation of the nucleus induced by NETosis. Moreover, a comparative study of NETosis induced by CaI and phorbol 12-myristate 13-acetate (PMA) revealed distinct phenotypes, with PMA-treated cells having significantly lower magnitude opacity and larger size than CaI-treated cells. The differential effects of each drug on the rates at which cells enlarge and exhibit altered membrane permeability due to NETosis may explain the differences. The results presented in both works by Petchakup *et al.* referred herein demonstrate the clear potential for integrating an analysis technique, such as impedance cytometry, with other relevant microfluidic sorting techniques, opening the door for truly point-of-care tools to be developed.

A different work also focusing on lymphocytes was presented by Rollo *et al.*, aiming at the electrical profiling of activated T-lymphocytes[79]. Adoptive T-cell immunotherapy is a promising approach in personalized medicine which requires the assessment of clonal antigen specificity followed by the label-free isolation of cells of interest. To assess if electrical phenotypes could indicate specific clonal antigen profiles, the authors analysed T-lymphocytes that were CD8+ unstimulated, CD8+ CD69+ activated, and CD8+ CD69- non-activated. Using a device comprised of 3D microelectrodes for signal acquisition (Fig. 2D), the impedance change associated with T-cell activation was measured using data at 6 and 14 MHz, where CD69+ cells presented a shift in the real component of impedance at both frequencies, possibly due to electrophysiology changes arising from activation processes, such as remodelling of actin cytoskeleton or the increment in nuclear volume (Fig. 7D).

Other mammalian cell types studied in recent literature include skeletal stem cells (SSCs) following enrichment and expansion[161]. SSCs are a rare population found in bone marrow with high capacity for bone and cartilage regeneration. The phenotypical profiling of these rare cells has the potential for sorting and enrichment of this population. The system integrated fluorescence detection for the identification of CD146+ cells, a key SSC surface marker. Impedance measurements showed that unexpanded SSCs were on average larger than other cells found in the bone marrow. Furthermore, following the *in vitro* culturing of SSCs for expansion, both cell size and membrane capacitance (assessed by magnitude opacity) increased significantly, as early as by passage 0 (Fig. 7E). SSCs also showed an increased membrane capacitance with osteogenic differentiation. However, when compared to other bone marrow cells, no significant differences in magnitude opacity were found with primary SSCs, thereby limiting membrane capacitance-based DEP enrichment. Nonetheless, the observed phenotypical differences in size and stiffness could be harnessed by other microfluidic techniques for SSCs enrichment, as explored in a subsequent work[167].

Another mammalian cell type studied recently was human umbilical vein endothelial cells (HUVECs), specifically utilized as model cells for the study of viability assessment after a hypertonic stimulus[119]. Loss of viability was induced by either a paraformaldehyde treatment or a heat-shock. The hypertonic stimulus (Fig. 5A) was implemented to cause volumetric differences between viable and non-viable cells, making the loss of viability detectable based on difference in impedance magnitude at low frequency (450 kHz) (Fig. 7F). The system presented comparable sensitivity in the assessment of viability to that of flow cytometry results. The system was capable of determining loss of viability through both paraformaldehyde and heat-shock methods, not only for HUVECs cell type, but also human colon cancer (HT-29) cells and immature bone-marrow-derived macrophages (iBMDM).

4.5 Human pathogens

Recent literature in the realm of impedance cytometry has also focused on the detection and phenotypical characterization of different human pathogenic organisms. An example is the work by McGrath *et al.* [151] focused on the analysis of waterborne parasitic protozoa, specifically from the *Cryptosporidium* and *Giardia* genus. Few techniques are capable of detecting and assessing the viability of single pathogens in a rapid manner[168], which is critical given that only 10 viable oocysts in a water sample can initiate a significant human infection. Measurements were performed comparing viable pathogens with heat-inactivated ones, which mimic naturally occurring non-viable oocysts. Due to the thick outer wall layer protecting oocysts, heat-inactivated cells undergo ion exchange with the suspending medium that causes a distinct electrophysiology difference versus untreated cells, as confirmed by the suspension of both sample types in a highly conductive medium (5× PBS) to optimize the discrimination. (Fig. 8A). Using data at high frequency (50 MHz), 2D Gaussian confidence ellipses were defined for each population, with the gating strategy involving the definition of a line of equal probability (*i.e.*, where detected events had equal probability of belonging to either population). This gating strategy resulted in the classification of the viability phenotype with over 90% certainty. Using the same strategy, discrimination between human pathogenic *C. parvum* and *G. lamblia* versus non-human pathogenic *C. muris* was also achieved with over 92% certainty, due to clear differences in cell size phenotypes.

Another system focused on waterborne pathogens developed a system to detect micron-scale human pathogenic bacteria in water samples[40]. Monitoring of bacterial concentrations is pivotal in water quality assessment, with 5 bacteria per mL being considered the permitted limit. Thus, the authors used impedance cytometry to identify bacteria suspended in tap water or an equivalent buffer of very low conductivity (0.085 S/m). Using reference polystyrene beads of 1 and 2 μm mixed with an *Escherichia coli* bacteria sample to demonstrate discrimination based on size differences at 200 kHz and impedance phase phenotypes at 7 MHz (Fig. 8B), different bacterial types within a mixed sample were discriminated, with the Gram-positive *Staphylococcus aureus* presenting higher impedance phase at 8 MHz than the Gram-negative *E. coli*. These results[40], [151] show the potential for an impedance-based system to be integrated in current water quality management for the detection of waterborne pathogens contaminations.

An additional work focused on the detection of bacterial phenotypes was recently presented by Moore *et al.*[153]. Gastrointestinal infections in hospital settings after antibiotic administration are widely attributed to the susceptibility of human microbiota to germination and colonization by *Clostridium difficile* (*C. difficile*). In this study, the metabolite conditions leading to germination of *C. difficile* spores was studied based on well separated high frequency (10 MHz) impedance phase signals from *C. difficile* in spore versus vegetative form (Fig. 8C), even though the impedance magnitude signal exhibited overlaps due to minimal size differences between spore aggregates and their vegetative form. In this manner, antibiotic-induced disruption of microbiota in a mouse model was shown to enhance susceptibility to spore germination.

Focusing on a different type of human pathogenic organisms, Honrado *et al.* performed the dielectric characterization of red blood cells infected by a malaria parasite[69]. Since malaria is the world's most prevalent parasitic disease, there is a need to understand the electrophysiological alterations of cells during the malaria infection cycle. To investigate this, the infection of RBCs by malaria parasites (*Plasmodium falciparum*) was followed, with measurements performed every 6 h post-invasion along the 48 h intraerythrocytic life cycle of the parasite. To identify the subpopulation of infected cells, GFP emitting parasites were utilized for integrated fluorescence detection. Impedance data at 5 MHz revealed the differing phenotype of infected versus uninfected cell populations (Fig. 8D). To probe the origin of the observed phenotypes, multi-shell modelling was performed to determine the dielectric properties of the cell and parasite at each individual time-point post-invasion. Analysis showed a significant increase in C_{mem} and σ_{cyt} of infected RBCs along the infection time course. These alterations are probably related with known membrane alterations caused by the parasite starting at early stages, which also influence the extent of ionic exchange between the intra- and extra-cellular regions. Alterations include changes to membrane lipid and protein composition, the expression of new pathways and the formation of angular elevations that alter membrane structure. Furthermore, the volume ratio taken by the parasite within the host cell was estimated to vary from less than 10% at earlier stages of infection to more than 90% at later stages. These findings can be used in future microfluidic sorting techniques for the enrichment and detection of infected cells.

4.6 Yeast Cells

A staple across the field of microfluidics is to utilize yeast cells (commonly from the *Saccharomyces cerevisiae* species) as a model sample type for testing of a variety of phenomena. Being easily accessible and culturable, yeast cells are optimal particles

to investigate size-based methods or explore new methods for viability assessment. On the latter point, Opitz *et al.* explored the utilization of impedance cytometry as a new quality control tool for the determination of cell viability and to assess cell culture status[72]. To mimic loss of viability, a heat-inactivation step was performed, with the estimated ratio of non-viable cells tracking well with standard flow cytometry methods, even in long-term batch cultures (Fig. 8E). By starving cells, the natural decay in viability was observed up to 18 days, with samples presenting a gradual decrease in impedance phase at 10 MHz. Cultures treated with the cytotoxic compound amphotericin showed a similar trend with increasing exposure times of up to 300 min. This phenotype of viability loss at 10 MHz is explained by the alterations in membrane properties upon death, resulting in changes to conductivity and capacitance for the cell membrane and internal structure.

The phenomenon of budding yeast has also gathered some interest in recent publications, as it works as a model for phenotyping strategies focused on morphology and shape, which can provide information about cellular physiological and pathological conditions. An example can be found in a recent work where single-cell morphology was assessed based on particle self-alignment[88] (Fig. 4B). Using signal width, amplitude and the ratio of width to amplitude (R) as metrics, unbudded yeast cells and early/late-budding cells were discriminated. By following the yeast proliferation process along 48h (Fig. 8F), it was observed that most cells are in the budding stage for the first 12h, however, from 24 h onward, the proportion of budding yeast is highly reduced, reaching a minimum at 48h. This state is comparable to the inactive, non-budding stage that yeast cells are commonly found at.

In another example, dielectrophoretic forces were used to trap budding yeast cells and perform size estimations of the trapped cells[132]. Eight trapping sites were defined to generate pressure differences capable of trapping the flowing particles. Electrical impedance spectroscopy was then performed on trapped particles. The size of trapped beads correlated well with impedance magnitude at 1 MHz. Hence, using the same metric, differences between single and budding yeast cells were observed, with the system being sensitive to variations in the size of the trapped particle. The capabilities to correctly identify the health and budding stage of cultures, presented in the herein highlighted literature, could possibly be applied in the fermentation industry as a rapid analysis technique.

4.7 Miscellaneous Biosystems

Besides the more traditional lines of work and applications for impedance cytometry, there have been some recent works focusing on less usual sample types or procedures. In one example by Heidman *et al.*[169], viability assessment of pollen from various species was studied: tobacco (*Nicotiana tabacum*), tomato (*Solanum lycopersicum*), cucumber (*Cucumis sativus*) and pepper (*Capsicum Annuum*). Pollen quality control is important for plant breeding research, and for plant and food production processes. Pollen viability is typically determined by classical methods, such as staining, but also using more laborious processes, like *in vitro* pollen germination. Impedance cytometry was thus explored by the authors as an alternative method for pollen analysis and viability assessment. Due to the large size of pollen particles, samples were run in microchannels with cross-sections of 120 × 120 μm (tobacco, tomato and pepper) or 250 × 250 μm (cucumber). Results showed that different stages of developing, viable, germinating and non-viable pollen populations could be detected and quantified based on differences in impedance phase between 3 and 12 MHz, with high correlation to other standard benchmarking methods. Moreover, pollen with active germination potential were also discriminated against non-viable pollen and non-germinating viable populations. These results suggest that impedance cytometry could then be adopted as an effective label-free technique for pollen quality control.

Another instance of an uncommon sample type is the green algae (*Picochlorum* SE3, Chlorophyta, 2 to 3 μm cell diameter), used for studies on viability assessment[55]. Algae were rendered non-viable with a 1h heat-treatment, with significant differences in magnitude opacity at 500 kHz and 20 MHz being observed. Non-viable cells presented smaller impedance magnitude at low and high frequencies, indicating a smaller size and altered cytoplasmic properties due to necrosis. Green algal cells were also cultured under different salinity conditions and analysed at different time points, with the magnitude opacity of cells being significantly reduced. Results suggest a capability by cells to adapt to the culturing conditions, which in turn suggests that this method could be implemented *in situ* to, not only analyse cell phenotype, but also assess the viability of cultures of varying media composition.

As a final example, while impedance cytometry has been widely used for label-free phenotyping of individual cells, it has yet to be used to detect larger biological systems or organisms. A recent case is the work by Zhu *et al.*, which reported the study of *C. elegans* using impedance cytometry[108]. *C. elegans* is a well-characterized model organism which has been widely used in genetic studies on developmental biology, aging and neurobiology. In this work, the authors explored impedance cytometry as a tool to identify the developmental stage (larval L1, L2, L3 and L4 stages or adult stage) of individual *C. elegans* worms. Using impedance magnitude data at 300 kHz, worm-length related parameters were correlated to developmental stage, since worms present specific body morphology, size and behaviour at each stage (Fig. 8G). The accuracy of phenotyping and identification varied between 82% to 97%, with later stages (L4 and adult) presenting optimal accuracy. Furthermore, small (*i.e.*, L1-L3) and large (*i.e.*, L4 and adult) worms, from a mixed population, were separated to different outlets by first performing a size-based discrimination step using impedance cytometry data, and then re-directing individual *C. elegans* to the desired outlet using a system of individually addressable valves. The system was not only capable of identifying specific developmental-related phenotypes, but also for integrating impedance data within a decision step for particle separation. These results show that impedance cytometry could have a broader spectrum of interest and applications, by integration

with separation technologies or by its application to sample types of larger scale.

5 Conclusions and outlook

The quantification of phenotypic heterogeneity is becoming increasingly significant to understand biological function and to address the needs of precision medicine. Over the last decade, microfluidic impedance cytometry has carved a niche within this broader need by enabling quantification of subpopulations based on their electrophysiology, especially for cell types that lack reliable biochemical markers to identify them. In recent years, novel design solutions have increased the accuracy of the technique and led to robust design-tailored tools to process the raw impedance signals. The capability of the technique to offer multiparametric information on the cells has also been enriched. It is now possible to acquire electrical fingerprints that convey biophysical information on cell size, shape, dielectric and mechanical properties, as well as on motion-related quantities such as cell velocity and position within the microchannel. Multifrequency measurements coupled with dielectric (multi-)shell models enable the quantification of conductivity and permittivity of subcellular features. Impedance spectroscopy of single flowing cells at up to eight simultaneous frequency has been demonstrated for identification by fitting of dielectric models, and microwave-based solutions are being developed to extend the frequency range, potentially enabling the identification of novel electrical biomarkers for the status of cell nucleus. Real-time processing of impedance data has also been shown, paving the way to inform sorting for downstream analysis of target sub-populations. Although cell sorting based on impedance-signature has been demonstrated[47,48,108], its great potential has not yet been fully exploited. Emerging microfabrication solutions, such as tubular microfluidics, are opening opportunities for electrical impedance tomography of flowing cells.

Some novel emerging directions in cell analysis include the development of impedance cytometers for single-bacteria analysis, by overcoming the challenges of downscaling to enable early diagnosis of bacterial infections, such as through gauging host microbiota susceptibility to infection and for reducing the timeframes for antibiotic susceptibility analysis. Recent advances highlight the importance of biophysical properties determined by impedance-based single-cell analysis to complement the biochemical information obtained from fluorescence-based flow cytometry, thereby enabling a more holistic picture of the cell phenotype, which is essential for understanding cell death mechanisms, elucidating cancer metastasis, and predicting stem cell differentiation lineage. We envision enhanced impedance-based deformability cytometry protocols by novel device designs and coupled modelling approaches to translate impedance metrics into biomechanical properties. Impedance-based platforms to monitor dynamic changes at the single-cell level after drug interventions to the same sample are also very promising.

Electric fields represent an invaluable tool for single-cell analysis and manipulation in microfluidic devices. Electrical sensing has the key advantage of being label-free while electrical forces scale favourably with miniaturization[170]. We envision the development of all-electrical integrated platforms wherein for instance: dielectrophoresis is used to manipulate cells[171] and other analytes[172–174]; impedance cytometry is used at multiple stations (*e.g.*, pre and post-stimuli) for dynamic cell biophysical characterization and cell tracking; electro-actuated valves[175] enable programmable flow control and sorting; selected cells undergo electrical lysis[176] and the released intracellular material is analysed on chip by means of impedance-based nanopores[177,178]. All-electrical systems show great promise for system integration and portability. The final goal is to design compact, modular and adaptive devices that use disposable chips and enable fast, user-friendly readout capabilities. This would enable the widespread use of the technology out-of-the-lab, within clinical settings, which is of central importance to validate newly discovered electrical biomarkers. A pivotal step in this direction would be the movement from cleanroom-based chip microfabrication to makerspace fabrication[179–181], which is getting closer thanks to developments in 3D printing, imprinting[182], flexible electronics and nanomaterials.

On the other hand, in order to stratify cell subpopulations in complex heterogeneous samples, novel hybrid microfluidic platforms could be developed, wherein electrical sensing is coupled *e.g.* with optical and fluorescence imaging[183,184], Raman[185] and hyperspectral[186] imaging, digital holography[187], and biochemical assays[188]. In fact, probing complementary cell properties (*e.g.*, morphological, biophysical, biochemical properties) enables multimodal sensing, which can significantly enhance the feature space used for cell characterization and discrimination. This comes with technical challenges in terms of device design and operation, as well as challenges in the combination of the acquired multimodal data[189,190]. Data streams from heterogeneous sensor sources can have different noise level, information content and representation (*e.g.*, structured vs unstructured data, 1D or 2D signals), and multimodal information fusion still need to be improved in theories, methodologies and practical systems[191]. Furthermore, as high-dimensional data become available, the identification of subpopulations by manual gating becomes impractical and automated data-driven clustering strategies are required[192,193]. In particular, unsupervised clustering methods can enable the unbiased detection of novel subpopulations.

In this framework, synergistic research efforts involving microfluidics, sensor science and machine learning are expected to bring single-cell analysis to its next level, with a tremendous impact for life-science research, diagnostics and personalized medicine.

Conflicts of interest

There are no conflicts to declare.

Acknowledgements

F.C. and P.B. acknowledge support from MIUR Grant (SIR Programme): RBSI14TX20. N.S. and C.H. acknowledge support from NIH Grants: 1R21AI130902-01 and NCATS UL1TR003015. The content is solely the responsibility of the authors and does not necessarily represent the official views of the National Institutes of Health. Illustrations from SMART—Servier Medical Art, Servier, were used on Figure 1 under the Creative Commons Attribution 3.0 Unported License.

References

1 S. Rubakhin, E. V. Romanova, P. Nemes and J. V. Sweedler, *Nat. Methods*, 2011, **8**, S20–S29.
2 K. Klepárník and F. Foret, *Anal. Chim. Acta*, 2013, **800**, 12–21.
3 J. Cros, J. Raffenne, A. Couvelard and N. Poté, *Pathobiology*, 2018, **85**, 64–71.
4 J. B. Mitchell, K. McIntosh, S. Zvonic, S. Garrett, Z. E. Floyd, A. Kloster, Y. Di Halvorsen, R. W. Storms, B. Goh, G. Kilroy, X. Wu and J. M. Gimble, *Stem Cells*, 2006, **24**, 376–385.
5 K. Yoshimura, T. Shigeura, D. Matsumoto, T. Sato, Y. Takaki, E. Aiba-Kojima, K. Sato, K. Inoue, T. Nagase, I. Koshima, K. Gonda, I. Koshima and K. Gonda, *J. Cell. Physiol.*, 2006, **208**, 64–76.
6 T. Jiang, W. Liu, X. Lv, H. Sun, L. Zhang, Y. Liu, W. J. Zhang, Y. Cao and G. Zhou, *Biomaterials*, 2010, **31**, 3564–3571.
7 J. L. Nourse, J. L. Prieto, A. R. Dickson, J. Lu, M. M. Pathak, F. Tombola, M. Demetriou, A. P. Lee and L. A. Flanagan, *Stem Cells*, 2014, **32**, 706–716.
8 A. Rohani, J. H. Moore, J. A. Kashatus, H. Sesaki, D. F. Kashatus and N. S. Swami, *Anal. Chem.*, 2017, **89**, 5757–5764.
9 Y. Liu and T. Ma, *Biotechnol. Prog.*, 2015, **31**, 468–481.
10 J. Skommer, T. Brittain and S. Raychaudhuri, *Apoptosis*, 2010, **15**, 1223–1233.
11 W. C. Lee, H. Shi, Z. Poon, L. M. Nyan, T. Kaushik, G. V. Shivashankar, J. K. Y. Chan, C. T. Lim, J. Han and K. J. Van Vliet, *Proc. Natl. Acad. Sci. U. S. A.*, 2014, **111**, E4409–E4418.
12 S. Gawad, K. Cheung, U. Seger, A. Bertsch and P. Renaud, *Lab Chip*, 2004, **4**, 241–251.
13 T. Sun and H. Morgan, *Microfluid. Nanofluid.*, 2010, **8**, 423–443.
14 T. B. Jones, *Electromechanics of Particles*, Cambridge University Press, 1995.
15 H. Morgan and N. G. Green, *AC Electrokinetics: Colloids and Nanoparticles*, Research Studies Press, 2003.
16 A. Hedayatipour, S. Aslanzadeh and N. McFarlane, *Biosens. Bioelectron.*, 2019, **143**, 111600.
17 A. Vembadi, A. Menachery and M. A. Qasaimeh, *Front. Bioeng. Biotechnol.*, 2019, **7**, 147.
18 D. Naranjo-Hernández, J. Reina-Tosina and M. Min, *J. Sensors*, 2019, **2019**, 9210258.
19 R. J. Yang, L. M. Fu and H. H. Hou, *Sensors Actuators, B Chem.*, 2018, **266**, 26–45.
20 T. Vaclavek, J. Prikryl and F. Foret, *J. Sep. Sci.*, 2019, **42**, 445–457.
21 M. Carminati, *J. Sensors*, 2017, **2017**, 7638389.
22 Y. Xu, X. Xie, Y. Duan, L. Wang, Z. Cheng and J. Cheng, *Biosens. Bioelectron.*, 2016, **77**, 824–836.
23 K. Galler, K. Bräutigam, C. Große, J. Popp and U. Neugebauer, *Analyst*, 2014, **139**, 1237–1273.
24 K. Heileman, J. Daoud and M. Tabrizian, *Biosens. Bioelectron.*, 2013, **49**, 348–359.
25 K. C. Cheung, M. Di Berardino, G. Schade-Kampmann, M. Hebeisen, A. Pierzchalski, J. Bocsi, A. Mittag and A. Tárnok, *Cytom. Part A*, 2010, **77**, 648–666.
26 J. Chen, C. Xue, Y. Zhao, D. Chen, M. H. Wu and J. Wang, *Int. J. Mol. Sci.*, 2015, **16**, 9804–9830.
27 C. Petchakup, K. H. H. Li and H. W. Hou, *Micromachines*, 2017, **8**, 87.
28 H. Daguerre, M. Solsona, J. Cottet, M. Gauthier, P. Renaud and A. Bolopion, *Lab Chip*, 2020, **20**, 3665–3689.
29 T. Sun, C. van Berkel, N. G. Green and H. Morgan, *Microfluid. Nanofluid.*, 2009, **6**, 179–187.
30 T. Sun, S. Gawad, C. Bernabini, N. G. Green and H. Morgan, *Meas. Sci. Technol.*, 2007, **18**, 2859–2868.
31 T. Sun, D. Holmes, S. Gawad, N. G. Green and H. Morgan, *Lab Chip*, 2007, **7**, 1034–1040.
32 C. Bernabini, D. Holmes and H. Morgan, *Lab Chip*, 2011, **11**, 407–412.
33 M. Evander, A. J. Ricco, J. Morser, G. T. A. Kovacs, L. L. K. Leung and L. Giovangrandi, *Lab Chip*, 2013, **13**, 722–729.
34 X. Zhu, K. W. Tung and P. Y. Chiou, *Appl. Phys. Lett.*, 2017, **111**, 143506.
35 N. Haandbæk, S. C. Bürgel, F. Heer and A. Hierlemann, *Lab Chip*, 2014, **14**, 369–377.
36 K. Cheung, S. Gawad and P. Renaud, *Cytom. Part A*, 2005, **65A**, 124–132.
37 N. Haandbæk, O. With, S. C. Bürgel, F. Heer and A. Hierlemann, *Lab Chip*, 2014, **14**, 3313–3324.
38 M. Kelleci, H. Aydogmus, L. Aslanbas, S. O. Erbil and M. Selim Hanay, *Lab Chip*, 2018, **18**, 463–472.
39 J.-C. Chien, A. Ameri, E.-C. Yeh, A. N. Killilea, M. Anwar and A. M. Niknejad, *Lab Chip*, 2018, **18**, 2065–2076.
40 C. H. Clausen, M. Dimaki, C. V. Bertelsen, G. E. Skands, R. Rodriguez-Trujillo, J. D. Thomsen and W. E. Svendsen, *Sensors (Switzerland)*, 2018, **18**, 3496.
41 M. Ostermann, A. Sauter, Y. Xue, E. Birkeland, J. Schoelermann, B. Holst and M. R. Cimpan, *Sci. Rep.*, 2020, **10**, 142.
42 E. J. W. Wynn and M. J. Hounslow, *Powder Technol.*, 1997, **93**, 163–175.
43 U. Hassan and R. Bashir, *Lab Chip*, 2014, **14**, 4370–4381.
44 F. Caselli, A. De Ninno, R. Reale, L. Businaro and P. Bisegna, *IEEE Trans Biomed Eng*, 2020, 10.1109/TBME.2020.2995364.
45 M. R. Kellman, F. R. Rivest, A. Pechacek, L. L. Sohn and M. Lustig, *IEEE Sens. J.*, 2018, **18**, 3068–3079.
46 N. Wang, R. Liu, N. Asmare, C. H. Chu and A. F. Sarioglu, *Lab Chip*, 2019, **19**, 3292–3304.
47 J. Schoendube, D. Wright, R. Zengerle and P. Koltay, *Biomicrofluidics*, 2015, **9**, 14117.

48 B. de Wagenaar, S. Dekker, H. L. de Boer, J. G. Bomer, W. Olthuis, A. Van Den Berg and L. I. Segerink, *Lab Chip*, 2016, **16**, 1514–1522.
49 X. Xie, Z. Cheng, Y. Xu, R. Liu, Q. Q. Li and J. Cheng, *Anal. Methods*, 2017, **9**, 1201–1212.
50 G. Salles-Loustau, T. Le, L. Najafizadeh, S. Zonouz and M. Javanmard, *Biomed. Microdevices*, 2018, **20**, 63.
51 A. Furniturewalla, M. Chan, J. Sui, K. Ahuja and M. Javanmard, *Microsystems Nanoeng.*, 2018, **4**, 20.
52 C. Raillon, J. Che, S. Thill, M. Duchamp, B. X. E. Desbiolles, A. Millet, E. Sollier and P. Renaud, *Cytom. Part A*, 2019, **95**, 1085–1095.
53 K. Ahuja, G. M. Rather, Z. Lin, J. Sui, P. Xie, T. Le, J. R. Bertino and M. Javanmard, *Microsystems Nanoeng.*, 2019, **5**, 34.
54 Z. Lin, S. Y. Lin, P. Xie, C. Y. Lin, G. M. Rather, J. R. Bertino and M. Javanmard, *Sci. Rep.*, 2020, **10**, 3015.
55 J. Sui, F. Foflonker, D. Bhattacharya and M. Javanmard, *Sci. Rep.*, 2020, **10**, 1251.
56 J. Sui, P. Xie, Z. Lin and M. Javanmard, *Talanta*, 2020, **215**, 120791.
57 S. Gawad, L. Schild and P. Renaud, *Lab Chip*, 2001, **1**, 76–82.
58 V. Errico, A. De Ninno, F. R. Bertani, L. Businaro, P. Bisegna and F. Caselli, *Sensors Actuators, B Chem.*, 2017, **247**, 580–586.
59 E. Valera, J. Berger, U. Hassan, T. Ghonge, J. Liu, M. Rappleye, J. Winter, D. Abboud, Z. Haidry, R. Healey, K. White and R. Bashir, *Lab Chip*, 2018, **18**, 1461–1470.
60 C. Petchakup, H. M. Tay, W. H. Yeap, R. Dalan, S. C. Wong, K. H. H. Li and H. W. Hou, *Biosens. Bioelectron.*, 2018, **118**, 195–203.
61 M. Serhatlioglu, M. Asghari, M. Tahsin Guler and C. Elbuken, *Electrophoresis*, 2019, **40**, 906–913.
62 A. Saateh, A. Kalantarifard, O. T. Celik, M. Asghari, M. Serhatlioglu and C. Elbuken, *Lab Chip*, 2019, **19**, 3815–3824.
63 C. Petchakup, H. M. Tay, K. H. H. Li and H. W. Hou, *Lab Chip*, 2019, **19**, 1736–1746.
64 A. De Ninno, R. Reale, A. Giovinazzo, F. R. Bertani, L. Businaro, P. Bisegna, C. Matteucci and F. Caselli, *Biosens. Bioelectron.*, 2020, **150**, 111887.
65 S. Dekker, P. K. Isgor, T. Feijten, L. I. Segerink and M. Odijk, *Microsystems Nanoeng.*, 2018, **4**, 34.
66 S. Emaminejad, S. Talebi, R. W. Davis and M. Javanmard, *IEEE Sens. J.*, 2015, **15**, 2715–2716.
67 P. Xie, X. Cao, Z. Lin, N. Talukder, S. Emaminejad and M. Javanmard, *Sens. Act. B Chem.*, 2017, **241**, 672–680.
68 T. Sun, N. G. Green, S. Gawad and H. Morgan, *IET Nanobiotechnol.*, 2007, **1**, 69–79.
69 C. Honrado, L. Ciuffreda, D. Spencer, L. Ranford-Cartwright and H. Morgan, *J. R. Soc. Interface*, 2018, **15**, 20180416.
70 G. Arrabito, V. Errico, A. De Ninno, F. Cavaleri, V. Ferrara, B. Pignataro and F. Caselli, *Langmuir*, 2019, **35**, 4936–4945.
71 J. S. McGrath, C. Honrado, J. H. Moore, S. J. Adair, W. B. Varhue, A. Salahi, V. Farmehini, B. J. Goudreau, S. Nagdas, E. M. Blais, T. W. Bauer and N. S. Swami, *Anal. Chim. Acta*, 2019, **1101**, 90–98.
72 C. Opitz, G. Schade, S. Kaufmann, M. Di Berardino, M. Ottiger and S. Grzesiek, *Appl. Microbiol. Biotechnol.*, 2019, **103**, 8619–8629.
73 D. Impe, J. Reitz, C. Köpnick, H. Rolletschek, A. Börner, A. Senula and M. Nagel, *Front. Plant Sci.*, 2020, **10**, 1588.
74 N. Demierre, T. Braschler, P. Linderholm, U. Seger, H. Van Lintel and P. Renaud, *Lab Chip*, 2007, **7**, 355–365.
75 A. Valero, T. Braschler and P. Renaud, *Lab Chip*, 2010, **10**, 2216–2225.
76 N. Demierre, T. Braschler, R. Muller and P. Renaud, *Sensors Actuators, B Chem.*, 2008, **132**, 388–396.
77 J. Cottet, A. Kehren, H. van Lintel, F. Buret, M. Frénéa-Robin and P. Renaud, *Microfluid. Nanofluidics*, 2019, **23**, 11.
78 S. C. C. Kilchenmann, E. Rollo, E. Bianchi and C. Guiducci, *Sens. Act. B Chem.*, 2013, **185**, 713–719.
79 E. Rollo, E. Tenaglia, R. Genolet, E. Bianchi, A. Harari, G. Coukos and C. Guiducci, *Biosens. Bioelectron.*, 2017, **94**, 193–199.
80 C. Grenvall, C. Antfolk, C. Z. Bisgaard and T. Laurell, *Lab Chip*, 2014, **14**, 4629–4637.
81 G. Mernier, E. Duqi and P. Renaud, *Lab Chip*, 2012, **12**, 4344–4349.
82 N. Haandbæk, S. C. Bürgel, F. Rudolf, F. Heer and A. Hierlemann, *ACS Sens*, 2016, **1**, 1020–1027.
83 M. Frankowski, J. Theisen, A. Kummrow, P. Simon, H. Ragusch, N. Bock, M. Schmidt and J. Neukammer, *Sensors (Switzerland)*, 2013, **13**, 4674–4693.
84 Y. Song, T. Zhou, Q. Liu, Z. Liu and D. Li, *Analyst*, , DOI:10.1039/d0an00679c.
85 W. Tang, D. Tang, Z. Ni, N. Xiang and H. Yi, *Anal. Chem.*, 2017, **89**, 3154–3161.
86 I. Bilican, M. T. Guler, M. Serhatlioglu, T. Kirindi and C. Elbuken, *Sensors Actuators, B Chem.*, 2020, **307**, 127531.
87 Y. Zhang, H. Liang, H. Tan, D. Chen, Y. Wang, Y. Xu, J. Wang and J. Chen, *Sensors Actuators, B Chem.*, 2020, **317**, 128231.
88 X. Xie, Z. Zhang, X. Ge, X. Zhao, L. Hao, Z. Cheng, W. Zhou, Y. Du, L. Wang, F. Tian, F. Tian and X. Xu, *Anal. Chem.*, 2019, **91**, 13398–13406.
89 D. Spencer and H. Morgan, *ACS Sensors*, 2020, **5**, 423–430.
90 D. Spencer, F. Caselli, P. Bisegna and H. Morgan, *Lab Chip*, 2016, **16**, 2467–2473.
91 A. De Ninno, V. Errico, F. R. Bertani, L. Businaro, P. Bisegna and F. Caselli, *Lab Chip*, 2017, **17**, 1158–1166.
92 A. De Ninno, R. Reale, A. Giovinazzo, F. R. Bertani, L. Businaro, P. Bisegna, C. Matteucci and F. Caselli, *Biosens. Bioelectron.*, 2019, 111887.
93 R. Reale, A. De Ninno, L. Businaro, P. Bisegna and F. Caselli, *Lab Chip*, 2019, **19**, 1818–1827.
94 F. Caselli, A. De Ninno, R. Reale, L. Businaro and P. Bisegna, *Sensors Actuators B. Chem.*, 2018, **256**, 580–589.
95 H. Wang, N. Sobahi and A. Han, *Lab Chip*, 2017, **17**, 1264.
96 D. Yang and Y. Ai, *Lab Chip*, 2019, **19**, 3609–3617.
97 M. Solsona, E. Y. Westerbeek, J. G. Bomer, W. Olthuis and A. Van Den Berg, *Lab Chip*, 2019, **19**, 1054–1059.

98 B. Brazey, J. Cottet, A. Bolopion, H. Van Lintel, P. Renaud and M. Gauthier, *Lab Chip*, 2018, **18**, 818–831.
99 R. Reale, A. De Ninno, L. Businaro, P. Bisegna and F. Caselli, *Microfluid. Nanofluidics*, 2018, **22**, 1–13.
100 C. Honrado, J. S. McGrath, R. Reale, P. Bisegna, N. S. Swami and F. Caselli, *Anal. Bioanal. Chem.*, 2020, **412**, 3835–3845.
101 C.-C. Chung, I.-F. Cheng, H.-M. Chen, H.-C. Kan, W.-H. Yang and H.-C. Chang, *Anal. Chem.*, 2012, **84**, 3347–3354.
102 J. Choi, J. Yoo, M. Lee, E.-G. Kim, J. S. Lee, S. Lee, S. Joo, S. H. Song, E.-C. Kim, J. C. Lee, Y.-G. Jung and S. Kwon, *Sci. Transl. Med.*, 2014, **6**, 267ra174.
103 A. Rohani, J. H. Moore, Y.-H. Su, V. Stagnaro, C. Warren and N. S. Swami, *Sensors Actuators, B Chem.*, 2018, **276**, 472–480.
104 D. Porro, M. Vai, M. Vanoni, L. Alberghina and C. Hatzis, *Cytom. Part A*, 2009, **75**, 114–120.
105 Z. Zhu, X. Xu, L. Fang, D. Pan and Q.-A. Huang, *Sens. Act. B Chem.*, 2016, **235**, 515–524.
106 K. L. Chen, M. M. Crane and M. Kaeberlein, *Mech. Ageing Dev.*, 2017, **161**, 262–269.
107 M. Shaker, L. Colella, F. Caselli, P. Bisegna and P. Renaud, *Lab Chip*, 2014, **14**, 2548–2555.
108 Z. Zhu, W. Chen, B. Tian, Y. Luo, J. Lan, D. Wu, D. Chen, Z. Wang and D. Pan, *Sensors Actuators, B Chem.*, 2018, **275**, 470–482.
109 F. Caselli, P. Bisegna and F. Maceri, *J. Microelectromechanical Syst.*, 2010, **19**, 1029–1040.
110 J. Wang, D. Karnaushenko, M. Medina-Sánchez, Y. Yin, L. Ma and O. G. Schmidt, *ACS Sensors*, 2019, **4**, 1476–1496.
111 S. M. Weiz, M. Medina-Sánchez and O. G. Schmidt, *Adv. Biosyst.*, 2018, **2**, 1870011.
112 D. Di Carlo, *J. Lab. Autom.*, 2012, **17**, 32–42.
113 Y. Zheng, J. Nguyen, C. Wang and Y. Sun, *Lab Chip*, 2013, **13**, 3275–3283.
114 M. Urbanska, H. E. Muñoz, J. Shaw Bagnall, O. Otto, S. R. Manalis, D. Di Carlo and J. Guck, *Nat. Methods*, 2020, **17**, 587–593.
115 D. Yang, Y. Zhou, Y. Zhou, J. Han and Y. Ai, *Biosens. Bioelectron.*, 2019, **133**, 16–23.
116 Y. Zhou, D. Yang, Y. Zhou, B. L. Khoo, J. Han and Y. Ai, *Anal. Chem.*, 2018, **90**, 912–919.
117 X. Ren, P. Ghassemi, J. S. J. S. Strobl and M. Agah, *Biomicrofluidics*, 2019, **13**, 044103.
118 P. Ghassemi, K. S. Harris, X. Ren, B. M. Foster, C. D. Langefeld, B. A. Kerr and M. Agah, *Sensors Actuators, B Chem.*, 2020, **321**, 128522.
119 Q. Zi, W. Ding, C. Sun, S. Li, D. Gao, L. He, J. Liu, L. Xu and B. Qiu, *Biosens. Bioelectron.*, 2020, **148**, 111820.
120 R. Reale, A. De Ninno, L. Businaro, P. Bisegna and F. Caselli, *Electrophoresis*, 2019, **40**, 1400–1407.
121 K. Chawla, M. M. Modena, P. S. Ravaynia, F. C. Lombardo, M. Leonhardt, G. Panic, S. C. Bürgel, J. Keiser and A. Hierlemann, *ACS Sensors*, 2018, **3**, 2613–2620.
122 P. S. Ravaynia, F. C. Lombardo, S. Biendl, M. A. Dupuch, J. Keiser, A. Hierlemann and M. M. Modena, *Adv. Biosyst.*, 2020, **4**, 1900304.
123 D. Holmes and H. Morgan, *Anal. Chem.*, , DOI:10.1021/ac902568p.
124 S. I. Han and K. H. Han, *Anal. Chem.*, , DOI:10.1021/acs.analchem.5b03147.
125 R. Liu, C.-H. Chu, N. Wang, T. Ozkaya-Ahmadov, O. Civelekoglu, D. Lee, A. K. M. Arifuzzman and A. F. Sarioglu, *Small*, 2019, **15**, 1904732.
126 R. Reale, A. De Ninno, M. A. Brighetti, L. Businaro, A. Travaglini, P. Bisegna and F. Caselli, in *23nd International Conference on Miniaturized Systems for Chemistry and Life Sciences (MicroTAS 2019)*, 2019.
127 Y. Liu, K. Wang, X. Sun, D. Chen, J. Wang and J. Chen, *Microfluid. Nanofluidics*, 2020, **24**, 45.
128 K. Chawla, S. C. Bürgel, G. W. Schmidt, H.-M. Kaltenbach, F. Rudolf, O. Frey and A. Hierlemann, *Microsystems Nanoeng.*, 2018, **4**, 8.
129 Y. Feng, L. Huang, P. Zhao, F. Liang and W. Wang, *Anal. Chem.*, 2019, **91**, 15204–15212.
130 V. Farmehini, W. Varhue, A. Salahi, A. R. Hyler, J. Čemažar, R. Davalos and N. S. Swami, *IEEE Trans. Biomed. Eng.*, 2019, 1.
131 W. Fan, X. Chen, Y. Ge, Y. Jin, Q. Jin and J. Zhao, *Biosens. Bioelectron.*, 2019, **145**, 111730.
132 Y. Geng, Z. Zhu, Y. Wang, Y. Wang, S. Ouyang, K. Zheng, W. Ye, Y. Fan, Z. Wang and D. Pan, *Electrophoresis*, 2019, **40**, 1436–1445.
133 M. Carminati, G. Ferrari, M. D. D. Vahey, J. Voldman and M. Sampietro, *IEEE Trans. Biomed. Circuits Syst.*, 2017, **11**, 1438–1449.
134 S. Dekker, W. Buesink, M. Blom, M. Alessio, N. Verplanck, M. Hihoud, C. Dehan, W. César, A. Le Nel, A. van den Berg and M. Odijk, *Sensors Actuators, B Chem.*, 2018, **272**, 468–478.
135 S. Zhang, Z. Li and Q. Wei, *Nanotechnol. Precis. Eng.*, 2020, **3**, 32–42.
136 M. A. Mansor, M. Takeuchi, M. Nakajima, Y. Hasegawa and M. R. Ahmad, *Appl. Sci.*, 2017, **7**, 170.
137 J. Panwar and R. Roy, *Microelectron. Eng.*, 2019, **215**, 111010.
138 Y. Fu, Q. Yuan and J. Guo, *Microfluid. Nanofluidics*, 2017, **21**, 20.
139 S. Prakash, B. K. Ashley, P. S. Doyle and U. Hassan, *Sci. Rep.*, 2020, **10**, 6109.
140 F. Caselli and P. Bisegna, *IEEE Trans Biomed Eng*, 2016, **63**, 415–422.
141 R. Liu, N. Wang, N. Asmare and A. F. Sarioglu, *Biosens. Bioelectron.*, 2018, **120**, 30–39.
142 R. Liu, N. Wang, F. Kamili and A. F. Sarioglu, *Lab Chip*, 2016, **16**, 1350–1357.
143 F. Caselli, A. De Ninno, R. Reale, L. Businaro and P. Bisegna, in *24nd International Conference on Miniaturized Systems for Chemistry and Life Sciences (MicroTAS 2020)*, 2020.
144 T. Sun, N. G. Green and H. Morgan, *NANO Br. Reports Rev.*, 2008, **3**, 55–63.
145 K. Mahesh, M. M. Varma and P. Sen, *J. Micromechanics Microengineering*, 2019, **29**, 115001.
146 H. Li, C. Multari, C. Palego, X. Ma, X. Du, Y. Ning, J. Buceta, J. C. M. Hwang and X. Cheng, *Sensors Actuators, B Chem.*,

2018, **255**, 1614–1622.

147 K. R. Foster and H. P. Schwan, *CRC Crit. Rev. Biomed. Eng.*, 1989, **17**, 25–104.

148 F. Caselli and P. Bisegna, *Med. Eng. Phys.*, 2017, **48**, 81–89.

149 F. Caselli, R. Reale, N. A. Nodargi and P. Bisegna, *Micromachines*, 2017, **8**, 283.

150 J. Claudel, A. L. De Araujo and M. Nadi, *Sensors (Switzerland)*, 2019, **19**, 3366.

151 J. S. McGrath, C. Honrado, D. Spencer, B. Horton, H. L. Bridle and H. Morgan, *Sci. Rep.*, 2017, **7**, 2601.

152 J. H. Moore, C. Honrado, V. Stagnaro, G. Kolling, C. A. Warren and N. S. Swami, *ACS Infect. Dis.*, 2020, **6**, 1000–1007.

153 J. H. Moore, A. Salahi, C. Honrado, C. Warburton, C. A. Warren and N. S. Swami, *Biosens. Bioelectron.*, 2020, **166**, 112440.

154 Y. Zhao, K. Wang, D. Chen, B. Fan, Y. Xu, Y. Ye, J. Wang, J. Chen and C. Huang, *Biosens. Bioelectron.*, 2018, **111**, 138–143.

155 K. Mahesh, M. M. Varma and P. Sen, *Lab Chip*, 2020.

156 K. Wang, Y. Zhao, D. Chen, B. Fan, Y. Lu, L. Chen, R. Long, J. Wang and J. Chen, *Sci. Data*, 2017, **4**, 170015.

157 D. R. Gossett, W. M. Weaver, A. J. MacH, S. C. Hur, H. T. K. Tse, W. Lee, H. Amini and D. Di Carlo, *Anal. Bioanal. Chem.*, 2010, **397**, 3249–3267.

158 A. Dalili, E. Samiei and M. Hoorfar, *Analyst*, 2019, **144**, 87–113.

159 C. Wyatt Shields IV, C. D. C. D. Reyes, G. P. Lopez and G. P. López, *Lab Chip*, 2015, **15**, 1230–1249.

160 D. Spencer, V. Hollis and H. Morgan, *Biomicrofluidics*, 2014, **8**, 64124.

161 M. Xavier, M. C. De Andres, D. Spencer, R. O. C. Oreffo and H. Morgan, *J. R. Soc. Interface*, 2017, **14**, 20170233.

162 T.-K. Chiu, Y. Zhao, D. Chen, C.-H. Hsieh, K. Wang, W.-P. Chou, C.-J. Liao, H.-Y. Wang, B. Fan, J. Wang, J. Chen and M.-H. Wu, *Sensors Actuators, B Chem.*, 2017, **246**, 29–37.

163 Y. Zhang, Y. Zhao, D. Chen, K. Wang, Y. Wei, Y. Xu, C. Huang, J. Wang and J. Chen, *Analyst*, 2019, **144**, 1008–1015.

164 H. A. Svahn and A. Van Den Berg, *Lab Chip*, 2007, **7**, 544–546.

165 H. Liang, Y. Zhang, D. Chen, H. Tan, Y. Zheng, J. Wang and J. Chen, *Micromachines*, 2019, **10**, 740.

166 J. M. Meacham, K. Durvasula, F. L. Degertekin and A. G. Fedorov, *Sci. Rep.*, 2018, **8**, 3727.

167 M. Xavier, S. H. Holm, J. P. Beech, D. Spencer, J. O. Tegenfeldt, R. O. C. Oreffo and H. Morgan, *Lab Chip*, 2019, **19**, 513–523.

168 Y. H. Su, M. Tsegaye, W. Varhue, K. T. Liao, L. S. Abebe, J. A. Smith, R. L. Guerrant and N. S. Swami, *Analyst*, 2013, **139**, 66–73.

169 I. Heidmann, G. Schade-Kampmann, J. Lambalk, M. Ottiger and M. Di Berardino, *PLoS One*, 2016, **11**, 1–15.

170 R. Pethig, *Dielectrophoresis: Theory, Methodology and Biological Applications, First Edition*, Wiley, 2017.

171 J. Cottet, A. Kehren, S. Lasli, H. van Lintel, F. Buret, M. Frénéa-Robin and P. Renaud, *Electrophoresis*, 2019, **40**, 1498–1509.

172 R. E. Fernandez, B. J. Sanghavi, V. Farmehini, J. L. Chávez, J. Hagen, N. Kelley-Loughnane, C. F. Chou and N. S. Swami, *Electrochem. commun.*, 2016, **72**, 144–147.

173 J. H. Moore, W. B. Varhue, Y. H. Su, S. S. Linton, V. Farmehini, T. E. Fox, G. L. Matters, M. Kester and N. S. Swami, *Anal. Chem.*, 2019, **91**, 10424–10431.

174 A. Rohani, B. J. Sanghavi, A. Salahi, K.-T. Liao, C.-F. Chou and N. S. Swami, *Nanoscale*, 2017, **9**, 12124–12131.

175 Y. Arango, Y. Temiz, O. Gökçe and E. Delamarche, *Sci. Adv.*, 2020, **6**, eaay8305.

176 G. Mernier, W. Hasenkamp, N. Piacentini and P. Renaud, in *Procedia Engineering*, 2010, vol. 5, pp. 37–40.

177 K. Yokota, M. Tsutsui and M. Taniguchi, *RSC Adv.*, 2014, **4**, 15886–15899.

178 Y. Jiang and W. Guo, *Sci. Bull.*, 2015, **60**, 491–502.

179 S. Emaminejad, M. Javanmard, R. W. Dutton and R. W. Davis, *Lab Chip*, 2012, **12**, 4499–4507.

180 A. Kundu, C. Nattoo, S. Fremgen, S. Springer, T. Ausaf and S. Rajaraman, *RSC Adv.*, 2019, **9**, 8949–8963.

181 S. Hales, E. Tokita, R. Neupane, U. Ghosh, B. Elder, D. Wirthlin and Y. L. Kong, *Nanotechnology*, 2020, **31**, 172001.

182 A. Salahi, W. B. Varhue, V. Farmehini, A. R. Hyler, E. M. Schmelz, R. V. Davalos and N. S. Swami, *Anal. Bioanal. Chem.*, 2020, **412**, 3881–3889.

183 A. Kleiber, A. Ramoji, G. Mayer, U. Neugebauer, J. Popp and T. Henkel, *Lab Chip*, 2020, **20**, 1676–1686.

184 N. Nitta, T. Sugimura, A. Isozaki, H. Mikami, K. Hiraki, S. Sakuma, T. Iino, F. Arai, T. Endo, Y. Fujiwaki, H. Fukuzawa, M. Hase, T. Hayakawa, K. Hiramatsu, Y. Hoshino, M. Inaba, T. Ito, H. Karakawa, Y. Kasai, K. Koizumi, S. Lee, C. Lei, M. Li, T. Maeno, S. Matsusaka, D. Murakami, A. Nakagawa, Y. Oguchi, M. Oikawa, T. Ota, K. Shiba, H. Shintaku, Y. Shirasaki, K. Suga, Y. Suzuki, N. Suzuki, Y. Tanaka, H. Tezuka, C. Toyokawa, Y. Yalikun, M. Yamada, M. Yamagishi, T. Yamano, A. Yasumoto, Y. Yatomi, M. Yazawa, D. Di Carlo, Y. Hosokawa, S. Uemura, Y. Ozeki and K. Goda, *Cell*, 2018, **175**, 266-276.e13.

185 N. Nitta, T. Iino, A. Isozaki, M. Yamagishi, Y. Kitahama, S. Sakuma, Y. Suzuki, H. Tezuka, M. Oikawa, F. Arai, Y. Ozeki and K. Goda, *Nat. Commun.*, 2020, **11**, 3452.

186 N. Mehta, S. Shaik, R. Devireddy and M. R. Gartia, *J. Biomech. Eng.*, 2018, **140**, 020802.

187 F. Merola, P. Memmolo, L. Miccio, R. Savoia, M. Mugnano, A. Fontana, G. D'Ippolito, A. Sardo, A. Iolascon, A. Gambale and P. Ferraro, *Light Sci. Appl.*, 2017, **6**, e16241.

188 W. Chen, F. Shao and Y. Xianyu, *Small*, 2020, **16**, 1903388.

189 J. Kittler, M. Hatef, R. P. W. Duin and J. Matas, *IEEE Trans. Pattern Anal. Mach. Intell.*, 1998, **20**, 226–239.

190 J. Riordon, D. Sovilj, S. Sanner, D. Sinton and E. W. K. Young, *Trends Biotechnol.*, 2019, **37**, 310–324.

191 M.-H. Yang and J.-H. Tao, *Virtual Real. Intell. Hardw.*, 2019, **1**, 21–38.

192 R. V. Bruggner, B. Bodenmiller, D. L. Dill, R. J. Tibshirani and G. P. Nolan, *Proc. Natl. Acad. Sci. U. S. A.*, 2014, **111**, E2770–E2777.

193 P. Liu, S. Liu, Y. Fang, X. Xue, J. Zou, G. Tseng and L.

Konnikova, *Front. Cell Dev. Biol.*, 2020, **8**, 234.
194 S. P. Desai, A. Coston and A. Berlin, *IEEE Trans. Nanobioscience*, 2019, **18**, 369–372.
195 D. Holmes, D. Pettigrew, C. H. Reccius, J. D. Gwyer, C. Van Berkel, J. Holloway, D. E. Davies and H. Morgan, *Lab Chip*, 2009, **9**, 2881–2889.
196 C. Van Berkel, J. D. Gwyer, S. Deane, N. Green, J. Holloway, V. Hollis and H. Morgan, *Lab Chip*, 2011, **11**, 1249–1255.

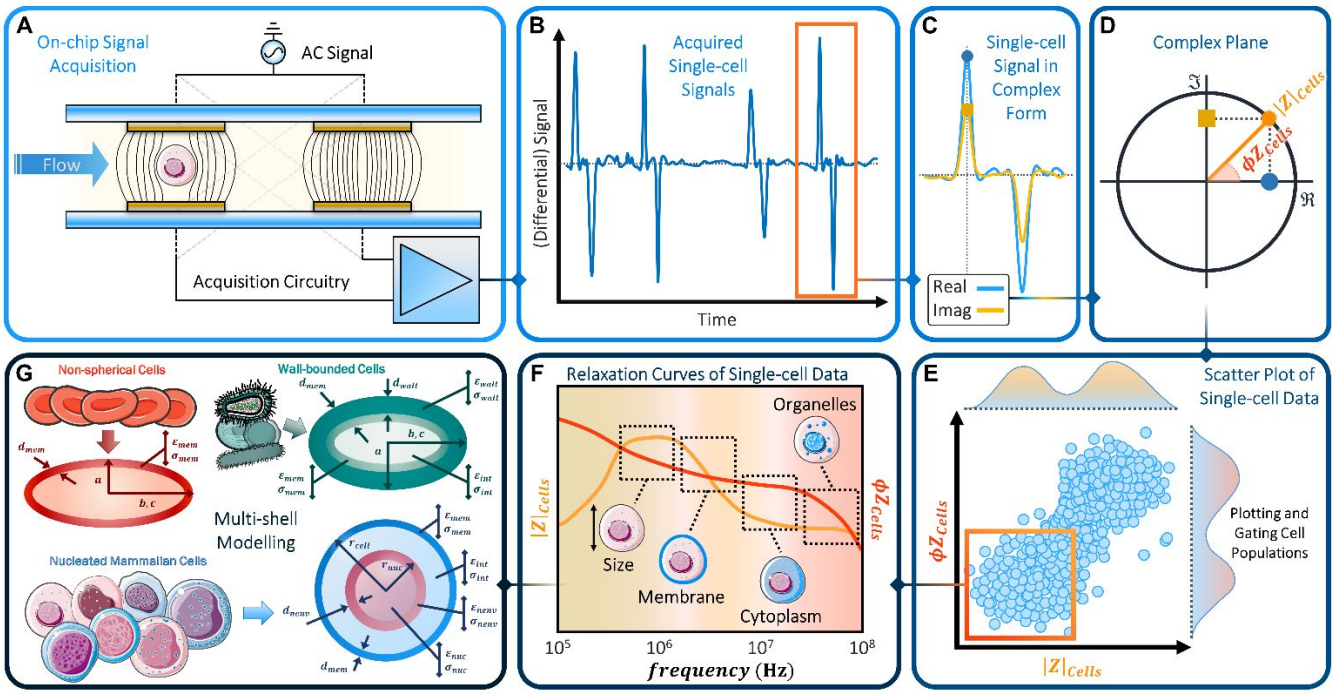

Fig. 1 Overview of impedance-based cell phenotyping. (A) Typical measurement setup: a multifrequency AC voltage signal is applied to the top electrodes and the differential current from the bottom electrodes is measured. (B) Acquired signal (real part, one frequency channel). (C) Single-cell signal (real and imaginary parts). Markers highlight peak values. (D) Peak amplitude representation in the complex plane, showing impedance magnitude (|Z|) and impedance phase (ϕZ). (E) Scatter plot of single-cell data (phase vs. magnitude). (F) Spectra of impedance magnitude and phase, with indication of the cellular features probed in each frequency range. (G) Multi-shell models used to fit the impedance spectra.

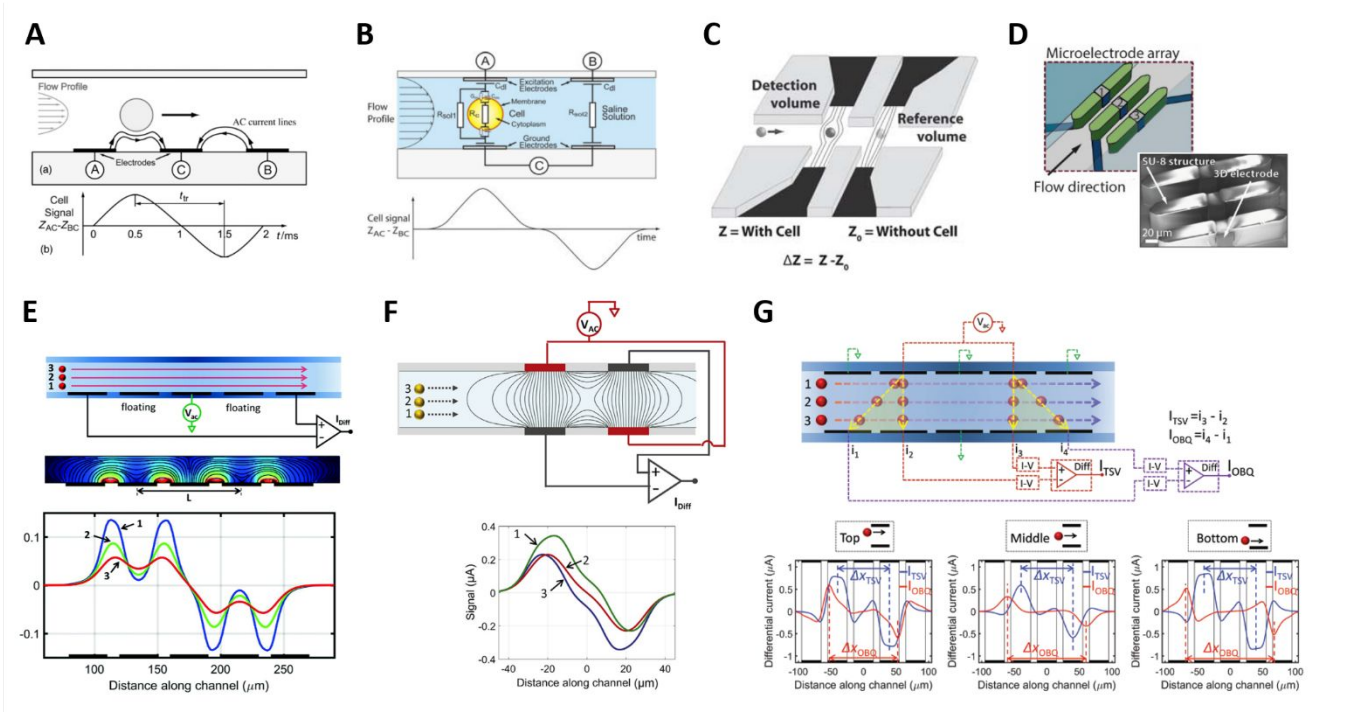

Fig. 2 (A) and (B) Classic coplanar and facing electrodes designs, respectively, along with relevant idealized signals. (C) *Liquid electrodes* concept. (D) Design based on three-dimensional electrodes. (E-G) Design enabling compensation of position blurring, along with simulated impedance traces for different particle trajectories. See Sections 2.2 and 2.3 for details. Images were adapted with permission from (A) ref. [57], copyright The Royal Society of Chemistry 2001, (B) ref. [36], copyright 2005 Wiley-Liss, Inc. (C) ref. [75], copyright The Royal Society of Chemistry 2010 (D) ref. [79], copyright 2017 Elsevier B.V. (E) ref. [58], copyright 2017 The Author(s), (F) ref. [94], copyright 2017 The Author(s), (G) ref. [90], copyright The Royal Society of Chemistry 2016.

Table 1 Overview of the microfluidic impedance cytometers discussed in Sections 2.4 and 2.5 (timeframe 2017-2020). References marked with an asterisk are further detailed in Table 2; if present, the relevant picture is indicated in brackets ('Ref.' column); MIC, microfluidic impedance cytometry; 'L-electrodes' indicates the liquid electrode concept (*i.e.*, metal electrodes recessed in lateral channels); N/A, not applicable.

A. Designs for electrical position detection			
Electrode layout	**Direction (and principle) of detection**	**Application**	**Ref.**
Single pair of non-parallel coplanar electrodes	Channel width (transit time)	Discrimination of five different transverse bead positions	Wang *et al.* 2017[95] (Fig. 3A)
3 N-shaped coplanar electrodes	Channel width (measured electrical signal and geometric relationships)	RBC/bead position detection, monitoring bead hydrodynamic focusing	Yang *et al.* 2019[96] (Fig. 3B)
2 facing electrode arrays	Channel width (gradient in electric field)	Bead tracking	Solsona *et al.* 2019[97] (Fig. 3C)
2 coplanar electrodes with non classical shape + DEP-focusing electrode array	Channel length (impedance variation)	Bead tracking (potentially real-time)	Brazey *et al.* 2018[98] (Fig. 3D)
Network of 10 code-multiplexed Coulter sensors	Location across 10 parallel channels (recognition of signal patterns)	Position detection of cells from different cell lines	Wang *et al.* 2019[46] (Fig. 3E)
5 coplanar L-electrode pairs + 5 coplanar electrodes	Channel width (ratio of transit times) + channel height (relative prominence)	Monitoring bead inertial focusing	Reale *et al.* 2018[99]
2 coplanar L-electrode pairs + 5 coplanar electrodes	Channel width (peak relative difference) + channel height (relative prominence)	Monitoring RBC/bead hydrodynamic focusing	Reale *et al.* 2019[93] (Fig. 3F)
2 coplanar L-electrode pairs + 2 facing electrode pairs	Channel width (peak relative difference) + channel height (peak relative difference)	RBC/yeast position detection	Honrado *et al.* 2020[100] (Fig. 3G)
B. Designs sensitive to cell shape or cell mechanical properties			
Electrode and fluidic layouts	**Impedance-based metrics**	**Application**	**Ref.**
1 coplanar electrode pair, 1 constriction structure	Pulse width, amplitude and width-to-amplitude ratio	Morphology-based yeast buddying analysis	Xie *et al.* 2019*[88] (Fig. 4B)
1 coplanar electrode pair, straight channel	Baseline-to-plateau current magnitude	Identification of developmental stages of *C. Elegans* with variable morphology	Zhu *et al.* 2018*[108]
4 coplanar electrode pairs, 1 constriction channel	3 passage times, impedance magnitude	Simultaneous electrical and mechanical cell characterization	Zhou *et al.* 2018*[116] (Fig. 4E)
1 coplanar electrode pair, 2 (or 5) constriction regions separated by 1 (or 4) relaxation region(s)	Signal features (transit times, rise times ratio, rise slope, impedance and phase drops)	Simultaneous electrical and mechanical cell characterization	Ren *et al.* 2019[117] (Fig. 4F), and Ghassemi *et al.* 2020[118]
4 three-dimensional electrodes, differential multiconstriction channel	4 transit times, relaxation index (*i.e.*, transit times ratio), average impedance magnitude	Simultaneous electrical and mechanical cell characterization	Yang *et al.* 2019*[115] (Fig. 4G)
C. Platforms with multiple electrical sensing zones			
MIC sensing zone (#, layout, wiring)	**Separating region(s)**	**Application**	**Ref.**
2 zones, 1 coplanar electrode pair each, absolute measurement	Hypertonic stimulation	Quantification of cell survival rate	Zi *et al.* 2020*[119] (Fig. 5A)
2 zones, 2 coplanar L-electrode pairs each, crossed differential wiring scheme	Dielectrophoresis	Monitoring dielectrophoretic focusing	Reale *et al.* 2019[120] (Fig. 5B)
2 zones, 3 coplanar electrodes each, differential measurement	Hyperbolic constriction	Coincidence arbitration	Caselli *et al.* 2020[44] (Fig. 5C)
2 zones, 2 coplanar electrodes each (1 in common), absolute measurement	N/A	Automated antischistosomal drug screening	Chawla *et al.* 2018[121]
2 zones, 3 coplanar electrodes each, differential measurement	Antigen specific capture chamber	Protein detection in undiluted plasma samples	Valera *et al.* 2018[59]
6 zones, 3 coplanar electrodes overall, shaped to create coded Coulter counters	Antigen specific capture chambers (4 overall)	Immunophenotyping against multiple antigens	Liu *et al.* 2019[125] (Fig. 5D)
D. Hybrid platforms			
MIC sensing zone (layout, wiring)	**Other sensing/manipulation modality**	**Application**	**Ref.**
2 coplanar L-electrode pairs, crossed differential wiring scheme	High-speed optical imaging of individual flowing cells	Multimodal analysis of pollen grains	Reale *et al.* 2019[126]
2 coplanar electrodes, absolute measurement	High-speed optical imaging of travelling single cell invading into a side constriction channel	Multiparametric cell characterization	Liu *et al.* 2020[127] (Fig. 5E)
2 coplanar electrodes, absolute measurement	Time-lapse microscopy of growing cells	Long-term monitoring of cell growth rates	Chawla *et al.* 2018[128] (Fig. 5F)
2 coplanar electrodes, absolute measurement	Impedance spectroscopy of individual trapped cells	Electrical property measurement of single cells	Feng *et al.* 2019*[129] (Fig. 5G)
2 coplanar electrodes, absolute measurement	Contactless dielectrophoretic particle manipulation	Increase robustness against chip-to-chip variability due to microfabrication errors	Farmehini *et al.* 2019[130]
2 coplanar electrodes, absolute measurement	Vortex chip	Isolation and enumeration of circulating tumour cells	Raillon *et al.* 2019[52] (Fig. 5H)
3 coplanar electrodes, differential measurement	Dean flow fractionation and flow rate reduction based on inertial focusing	Leukocyte isolation	Petchakup *et al.* 2019*[63] (Fig. 5I)
Interdigital electrodes (5 fingers)	Encapsulation of cells in droplets	Monitoring osteogenic differentiation	Fan *et al.* 2019[131]

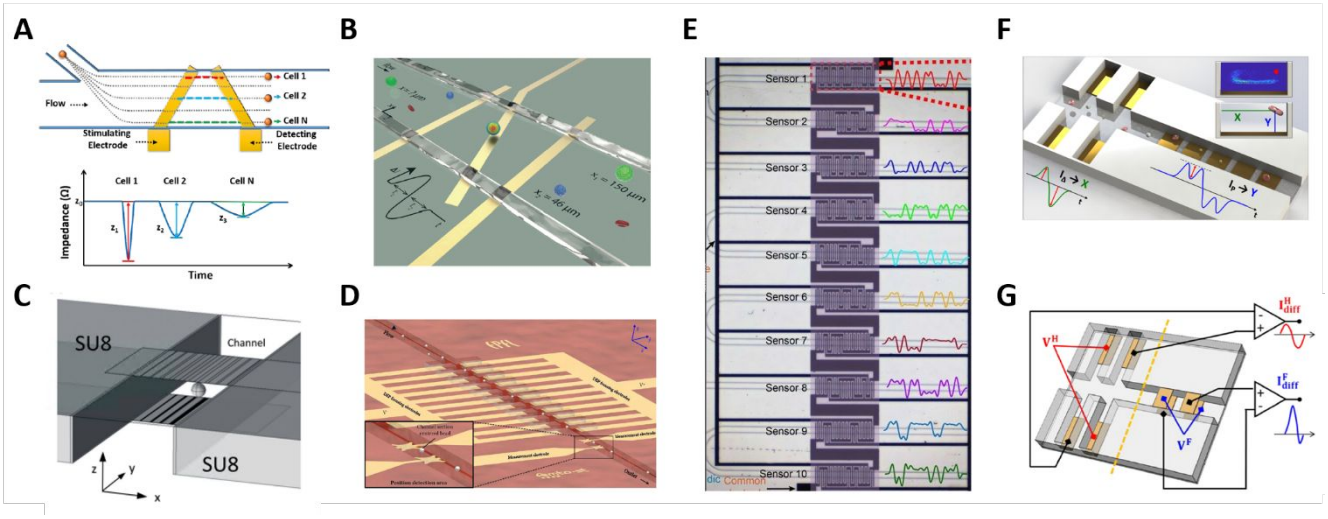

Fig. 3 (A-E) Systems for electrical position detection along one spatial coordinate. (F) and (G) Designs for cross-sectional position detection. See Section 2.3 and Table 1A. Images were adapted with permission from (A) ref. [95], copyright The Royal Society of Chemistry 2017, (B) ref. [96], copyright The Royal Society of Chemistry 2019 (C) ref. [97], copyright The Royal Society of Chemistry 2019 (D) ref. [98], copyright The Royal Society of Chemistry 2018 (E) ref. [46], copyright The Royal Society of Chemistry 2019 (F) ref. [93], copyright The Royal Society of Chemistry 2019, (G) ref. [100], copyright Springer-Verlag GmbH Germany, part of Springer Nature 2020.

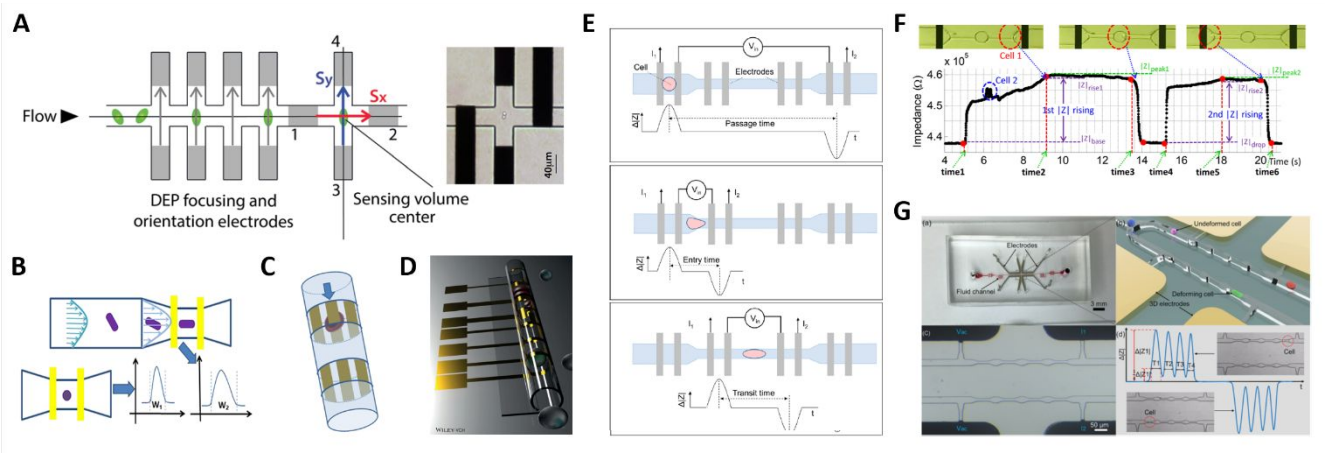

Fig. 4 (A-C) Shape-sensitive designs. (D) Microtubular channel with integrated electrodes. (E-G) Designs for mechanical characterization. See Section 2.4 and Table 1B for details. Images were adapted with permission from (A) ref. [107], copyright The Royal Society of Chemistry 2014, (B) ref. [88], copyright 2019 American Chemical Society, (C) ref. [109], copyright 2010 IEEE, (D) ref. [111], 2018 WILEY-VCH Verlag GmbH & Co. KGaA, Weinheim, (E) ref. [116], copyright 2017 American Chemical Society, (F) ref. [117], copyright 2019 Author(s), (G) ref. [115], copyright 2019 Elsevier B.V.

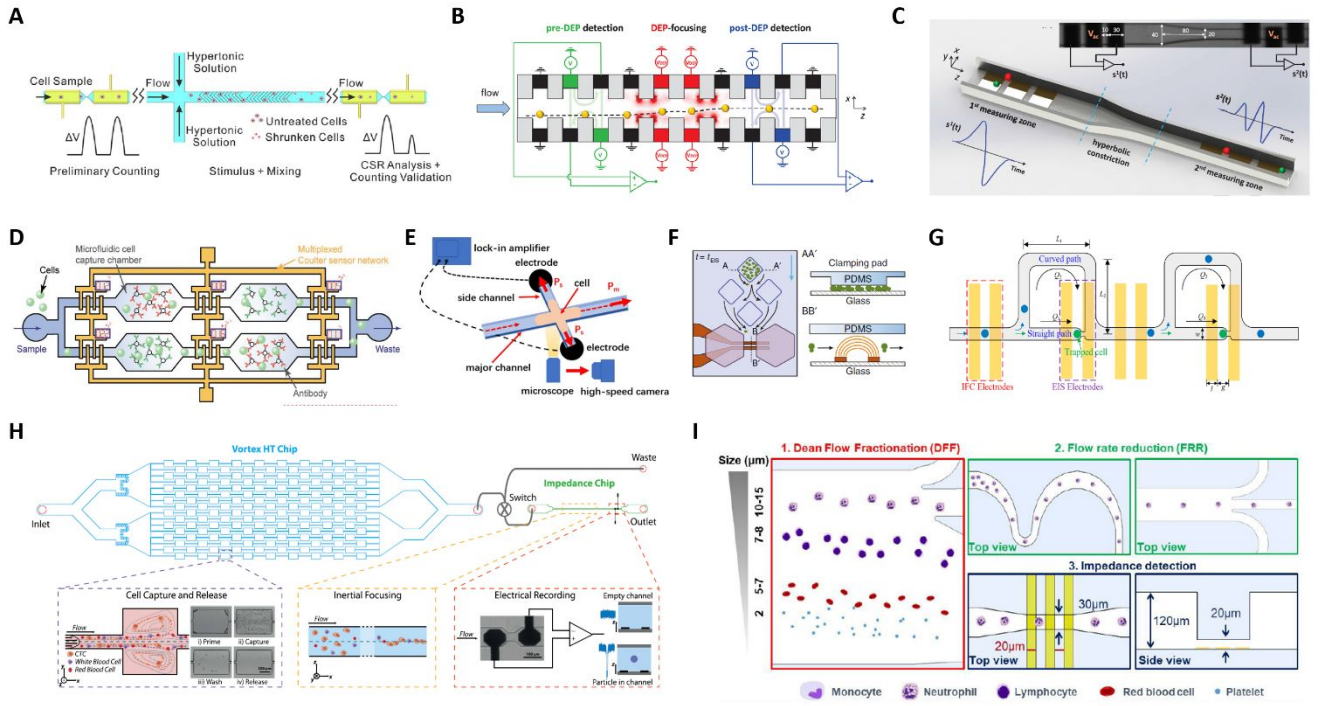

Fig. 5 (A-D) Platforms with two or more electrical sensing zones, which are separated by: (A) a region of hypertonic stimulation, (B) a region of dielectrophoretic focusing, (C) a hyperbolic constriction, and (D) antigen specific capture chambers. (E-I) Hybrid platforms combining impedance cytometry with: (E) high-speed optical imaging, (F) time-lapse microscopy of growing cells, (G) impedance spectroscopy of individual trapped cells, (H) a Vortex chip for selective enrichement, and (I) two inertial focusing stages for Dean flow fractionation and flow rate reduction, respectively. See Section 2.5 and Table 1C-D for details. Images were adapted with permission from (A) ref. [119], copyright 2019 Elsevier B.V, (B) ref. [120], copyright 2019 WILEY-VCH Verlag GmbH & Co. KGaA, Weinheim, (C) ref. [44], copyright 2020 IEEE, (D) ref. [125], 2019 WILEY-VCH Verlag GmbH & Co. KGaA, Weinheim, (E) ref. [127], copyright Springer-Verlag GmbH Germany, part of Springer Nature 2020, (F) ref. [128], copyright The Author(s) 2018, (G) ref. [129], copyright 2019 American Chemical Society, (H) ref. [52], copyright 2019 International Society for Advancement of Cytometry, (I) ref. [63], copyright The Royal Society of Chemistry 2019.

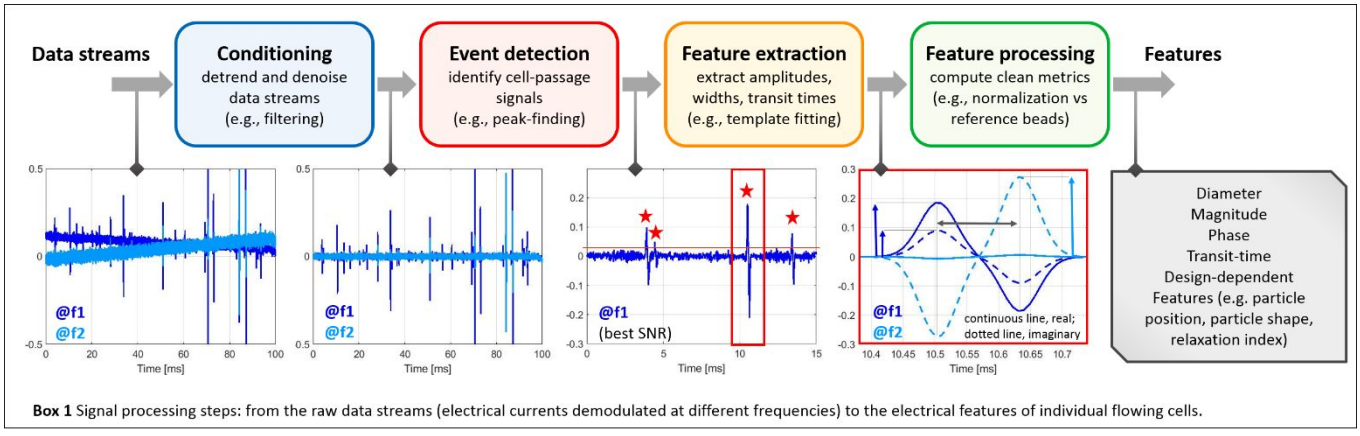

Box 1 Signal processing steps: from the raw data streams (electrical currents demodulated at different frequencies) to the electrical features of individual flowing cells.

A Equivalent circuit model (ECM) and Maxwell's mixture theory (MMT)

(i)

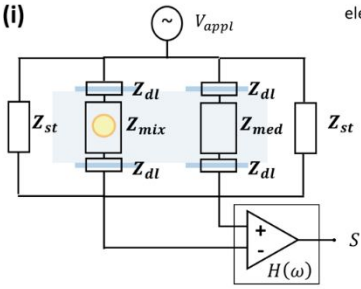

electrode **double-layer**

$$Z_{dl} = \frac{1}{j\omega C_{dl} A}$$

acquisition system **transfer function**

$$S = H(\omega) I_{diff}$$

neglecting stray capacitances Z_{st}

$$I_{diff} = \frac{V_{appl}}{2Z_{dl} + Z_{med}} - \frac{V_{appl}}{2Z_{dl} + Z_{mix}} \cong V_{appl} \frac{(Z_{mix} - Z_{med})}{(2Z_{dl} + Z_{med})^2}$$

introducing **MMT**

$$I_{diff} \cong -\frac{V_{appl}}{Z_{med}} \frac{1}{[1 + (2Z_{dl}/Z_{med})]^2} 3\varphi \tilde{f}_{CM}$$

(ii) ECM

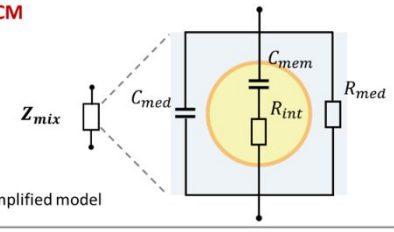

(iv) Single-shell model

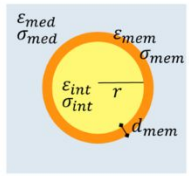

(iii) MMT

G **geometric factor** accounting for fringing
φ cell volume fraction, $\tilde{\varepsilon} = \varepsilon + \sigma/j\omega$

$$Z_{mix} = \frac{1}{j\omega \tilde{\varepsilon}_{mix} G} \qquad Z_{med} = \frac{1}{j\omega \tilde{\varepsilon}_{med} G}$$

Clausius-Mossotti factor

single-shell model, small d_{mem}/r

$$\tilde{\varepsilon}_{mix} = \tilde{\varepsilon}_{med} \frac{1 + 2\varphi \tilde{f}_{CM}}{1 - \varphi \tilde{f}_{CM}} \qquad \tilde{f}_{CM} = \frac{\tilde{\varepsilon}_{cell} - \tilde{\varepsilon}_{med}}{\tilde{\varepsilon}_{cell} + 2\tilde{\varepsilon}_{med}} \qquad \tilde{\varepsilon}_{cell} \cong \tilde{\varepsilon}_{int} \frac{\chi}{1 + \chi} \qquad \chi = \frac{\tilde{\varepsilon}_{mem}/d_{mem}}{\tilde{\varepsilon}_{int}/r}$$

simplified case ($\varepsilon_{med} = \varepsilon_{int} = 0, \sigma_{mem} = 0$), **Debye** relaxation: $\tilde{f}_{CM} = f_{CM.\infty} + \frac{f_{CM.0} - f_{CM.\infty}}{1 + j\omega\tau}$

$$f_{CM,\infty} = \frac{\sigma_{int} - \sigma_{med}}{\sigma_{int} + 2\sigma_{med}} \qquad f_{CM,0} = -\frac{1}{2} \qquad \tau = \frac{r\varepsilon_{mem}}{d_{mem}} \left(\frac{1}{\sigma_{int}} + \frac{1}{2\sigma_{med}} \right)$$

B Finite element model (FEM)

electrodes: distributed impedance

$$\boldsymbol{n} \cdot \boldsymbol{J} = j\omega C_{dl} (V - V_{appl})$$

$V_{appl} \neq 0$ on stimulating electrodes (e.g., 1 and 2)

$V_{appl} = 0$ on current collecting electrodes (e.g., 3 and 4)

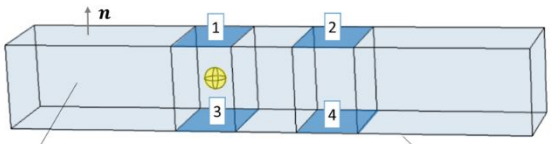

suspending medium: current conservation

$$\nabla \cdot \boldsymbol{J} = 0, \boldsymbol{J} = -(\sigma_{med} + j\omega\varepsilon_{med}) \nabla V$$

insulating boundary

$$\boldsymbol{n} \cdot \boldsymbol{J} = 0$$

intracellular space: current conservation

$$\nabla \cdot \boldsymbol{J} = 0, \boldsymbol{J} = -(\sigma_{int} + j\omega\varepsilon_{int}) \nabla V$$

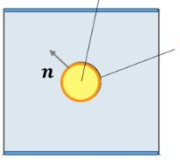

cell membrane: contact impedance

$$\boldsymbol{n} \cdot \boldsymbol{J}_{int} = \boldsymbol{n} \cdot \boldsymbol{J}_{med}$$

$$\boldsymbol{n} \cdot \boldsymbol{J}_{int} = \frac{1}{d_{mem}} (\sigma_{mem} + j\omega\varepsilon_{mem})(V_{int} - V_{med})$$

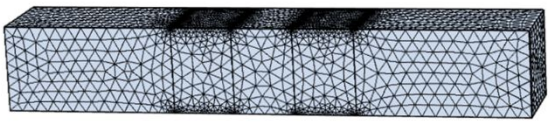

refine mesh where high field gradients are expected

post-processing:
current over i-th electrode

$$I_i = \iint_{\substack{electrode \\ surface}} \boldsymbol{n} \cdot \boldsymbol{J} \, dA$$

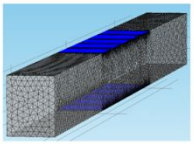

multielectrode designs: decouple FEM analysis and wiring scheme, by computing system admittance matrix $\boldsymbol{Y}$

Box 2 Overview of typical modelling approaches used in microfluidic impedance cytometry, with reference to the parallel facing electrode design in differential measurement configuration. Notation: subscripts $appl$ and $diff$ stand for applied and differential, respectively; subscripts int, mem and med refer to intracellular space, cell membrane and suspending medium, respectively; ω is the circular frequency; ε and σ denote permittivity and conductivity, respectively; r and d_{mem} denote cell radius and membrane thickness, respectively; $\boldsymbol{J}$ and V denoted electric current density and electric potential, respectively; $\boldsymbol{n}$ is the unit normal vector; ∇ and $(\nabla \cdot)$ denote gradient and divergence operators, respectively.

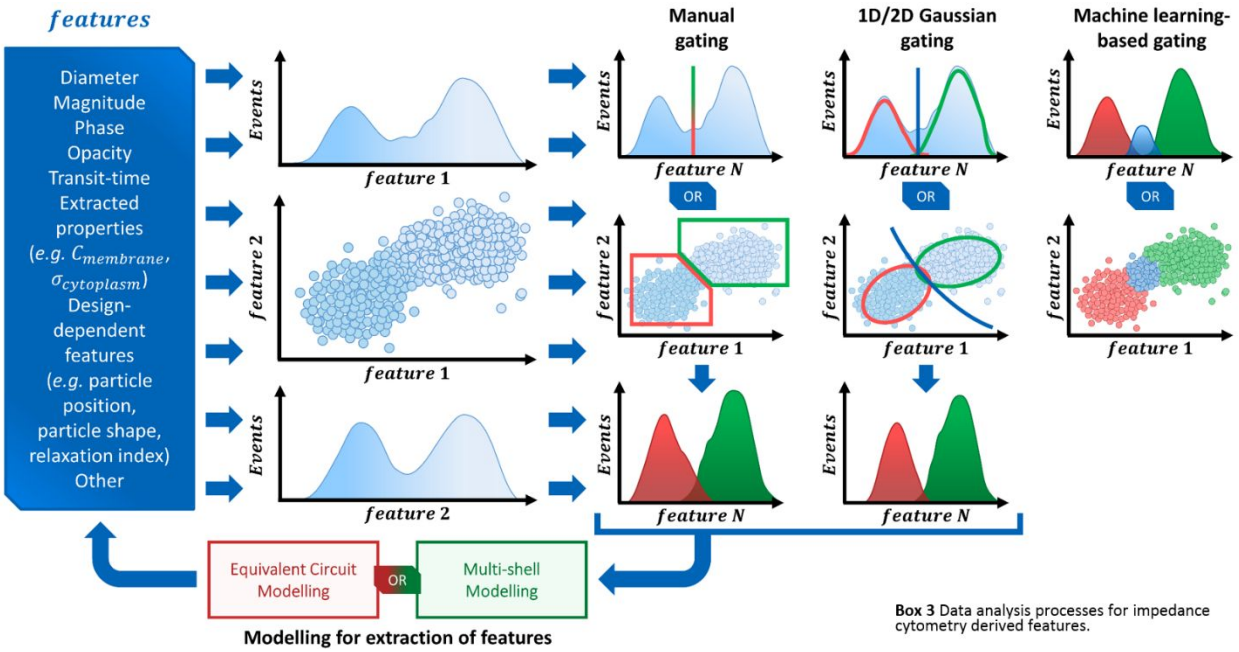

Box 3 Data analysis processes for impedance cytometry derived features.

Table 2 Overview of cell population phenotypical analysis using single-cell microfluidic impedance cytometry discussed in Section 4. *PS = polystyrene; †NCCD = No cell concentration declared; ‡NFRD = No flow-rate declared; §NSVD = No signal voltage declared.

Sample Type	Focus	Sample Composition	Sample Concentration/ Flow-rate/Cell Throughput	Acquisition Conditions (Frequencies, Voltage & Channel cross-section)	Characterization Metrics & Methods	Ref.
Algae	Viability assessment of bacterium-sized green algae	*Picochlorum* SE3 algae (~2–3 μm cell diameter); (ref. particles: *PS beads)	†NCCD ‡NFRD	500 kHz to 30 MHz (8 simultaneous frequencies) §NSVD 30 μm × 8 μm	Magnitude & Opacity (Magnitude 20 MHz/Magnitude 500 kHz)	Sui *et al.* 2020[55]
C. elegans	Identification of *C. elegans* developmental stages	*C. elegans* (~200 μm – 1.2 mm length)	†NCCD 30 μL/min	300 kHz 1.5 V amplitude 160 μm × 130 μm	Transit Time & Magnitude	Zhu *et al.* 2018[108]
Cancer Cells	Discrimination of dissociated tumour cell lines from major cancer types	Lung, thyroid, breast, ovarian, and kidney normal and cancer cells (~10–20 μm cell diameter); (testing particles: peripheral blood mononucleated cells, RBCs)	†NCCD 50 μL/min	250 kHz §NSVD 25 μm × 25 μm	Transit-time & Signal peak-to-peak voltage	Desai *et al.* 2019[194]
Cancer Cells	Characterization of phenotypical properties of circulating tumour cells	Lung cancer cell lines A549 and MLO-Y4; Isolated CTCs from hepatic, oral and lung cancer (~10–20 μm cell diameter)	2×10^4 cells/mL 50, 100 and 150 μL/h	1 kHz & 100 kHz §NSVD 6-10 μm × 6-10 μm	Transit-time, Magnitude, Phase & Dielectric Properties (C_{mem} & σ_{cyt}); Equivalent Circuit Models	Chiu *et al.* 2017[162]
Cancer Cells	Characterization of phenotypical properties of tumour cell lines	Lung cancer cell line A549, Adenoid carcinoma cell line SACC-83 and lung metastasis cell line SACC-LM (~10–20 μm cell diameter)	5×10^6 cells/mL ‡NFRD	100 kHz & 250 kHz §NSVD 11 μm × 9 μm	Transit-time, Magnitude, Phase & Dielectric Properties (C_{mem} & σ_{cyt}); Equivalent Circuit Models	Zhang *et al.* 2019[163]
Cancer Cells	Characterization of phenotypical properties of single-nuclei	Nuclei from cancer cell lines A549 and SW620	1×10^6 nuclei/mL ‡NFRD	1 kHz to 250 kHz 0.2 V amplitude 5-8 μm × 5-7 μm	Magnitude, Phase & Dielectric Properties (C_{ne}, R_{ne}, & R_{np}); Equivalent Circuit Models	Liang *et al.* 2019[165]
Cancer Cells	Characterization of pancreatic tumourigenicity phenotypes	Pancreatic tumour xenografts from metastatic (T366 and T608) vs. primary cancer of mutant genotype (T449 and T395) and wild type (T738 and T188) (~12–20 μm cell diameter); (ref. particles: 7 μm *PS beads)	2×10^5 cells/mL 1.2×10^5 beads/mL 100 μL/min	500 kHz, 18.3 MHz & 250 kHz to 50 MHz (24 frequencies) 6 V amplitude 60 μm × 30 μm	Real, Imaginary, Magnitude, Phase, Electrical Diameter, Opacity (Magnitude 2MHz/Magnitude 500 kHz) & Contrast (Phase 50MHz/Phase 500kHz); 2D Gaussian gating	McGrath *et al.* 2019[71]
Cancer Cells	Characterization of phenotypical properties of tumour cell lines with epithelial-mesenchymal transitions.	Lung cancer cell lines A549 & H1299; (testing particles: HeLa model cell line) (~10–40 μm cell diameter)	3-5 × 10^6 cells/mL ‡NFRD	100 kHz & 250 kHz §NSVD 10 μm × 12 μm	Transit-time, Magnitude, Phase & Dielectric Properties (C_{mem} & σ_{cyt}); Equivalent Circuit Models & Neural Network Pattern Recognition (two-layer feed forward)	Zhao *et al.* 2018[154]
Human Pathogens	Detection and enumeration of Gram-positive and Gram-negative bacteria	Gram-positive *Staphylococcus aureus* and Gram-negative *Escherichia coli* (~1 μm cell diameter and 2-3 μm × 0.5 μm, respectively); (ref. particles: 1 and 2 μm *PS beads)	2-2.5 × 10^6 particles/mL 0.01 μL/min	200 kHz, 7 MHz & 8 MHz 3 V amplitude 10 μm × 10 μm	Magnitude, Phase & Opacity (Magnitude 7 MHz / Magnitude 200 kHz)	Clausen *et al.* 2018[40]
Human Pathogens	Viability assessment and species discrimination of water-borne pathogens	*Cryptosporidium parvum*, *Cryptosporidium muris* and *Giardia lamblia* (~4 μm, ~6 μm and 9 μm cell diameter, respectively); (ref. particles: 7 μm *PS beads)	1×10^5 cells/mL 1×10^5 beads/mL 40 μL/min	18.3 MHz & 250 kHz to 50 MHz (24 frequencies) 1 to 10 V amplitude 40 μm × 30 μm	Real, Imaginary, Magnitude & Phase; 2D Gaussian gating & Multi-shell Modelling	McGrath *et al.* 2017[151]
Human Pathogens	Characterization of phenotypical properties of *Plasmodium falciparum*-infected RBCs	*Plasmodium falciparum*-infected RBCs and uninfected RBCs (~7.5 μm × 2 μm); (ref. particles: 7 μm *PS beads)	5×10^5 cells/mL 1×10^5 beads/mL 40 μL/min	18.3 MHz & 250 kHz to 50 MHz (24 frequencies) §NSVD 40 μm × 30 μm	Real, Imaginary, Magnitude, Phase & Fluorescence; Multi-shell Modelling	Honrado *et al.* 2018[69]
Human Pathogens	Detection of susceptibility of host microbiota to bacterial spore germination	*Clostridioides difficile* in spore and vegetative form (~0.5 μm diameter and ~2-5 μm × 0.5 μm, respectively); (ref. particles: 2 μm *PS beads)	†NCCD 10 μL/min	0.5, 2 & 10 MHz 0.5 V amplitude 30 μm × 30 μm	Magnitude & Phase	Moore *et al.* 2020[153]
HUVECs	Viability assessment of hypertonic stimulated cells	Human umbilical vein endothelial cells – HUVECs, human colon cancer (HT-29) cells and immature bone-marrow-derived macrophages (iBMDM) (~10–20 μm cell diameter); (testing particles: 5, 10 and 15 μm *PS beads)	1×10^5 cells/mL 0.3-1.7 × 10^5 beads/mL 20 μL/min	450 kHz 5 V amplitude 20 μm × 20 μm	Magnitude	Zi *et al.* 2020[119]
Model Cell Lines	Discrimination of live, necrotic and apoptotic cells	HeLa and Jurkat model cell lines (~10–40 μm cell diameter); (ref. particles: 3, 5, 7 and 10 μm *PS beads)	1-10 × 10^6 particles/mL -200 μL/min	1 MHz 0.3 V amplitude 25 μm × 12 μm	Conductance, Susceptance, Magnitude & Phase	Xie *et al.* 2017[49]
Model Cell Lines	Combined impedance flow cytometry (IFC) and electrical impedance spectroscopy (EIS) for cell analysis	HeLa, HepG2 and A549 model cell lines (~10–40 μm cell diameter); (ref. particles: 6 μm *PS beads)	1×10^6 cells/mL 10 nL/min	IFC: 1 MHz EIS: 1 – 10^3 kHz 1 V amplitude 30 μm × 20 μm	Magnitude; Equivalent Circuit Models	Feng *et al.* 2019[129]

Model Cell Lines	Discrimination of live, necrotic and apoptotic cells	Lymphoma model cell line U937 (~13 μm cell diameter); (ref. particles: 10 μm *PS beads)	†NCCD ‡NFRD	500 kHz, 2 MHz, 6 MHz & 12 MHz §NSVD 50 μm × 50 μm	Magnitude & Phase	Ostermann *et al.* 2020[41]
Model Cell Lines	Discrimination of live, necrotic and apoptotic cells	Lymphoma model cell line U937 (~13 μm cell diameter); (ref. particles: 6 μm *PS beads)	10 μL/min 200 cells/s	500 kHz & 10 MHz 5 V amplitude 40 μm × 21 μm	Electrical diameter & Phase; Multi-shell Modelling	De Ninno *et al.* 2020[64]
Model Cell Lines	Characterization of deformability and impedance phenotypes of cancer cells	Normal, fixed and PMA-modified model MCF-7 cells (~15-25 μm cell diameter); (ref. particles: RBCs)	0.5-1 × 10^6 cells/mL 1000 cells/min	1 MHz 0.5 V amplitude 10 μm × 20 μm	Time metrics & Magnitude	Zhou *et al.* 2018[116]
Model Cell Lines	Characterization of biophysical and impedance phenotypes of cancer cells	Model cell lines (H460, H446, A549, 95D and 95C) (~10–20 μm cell diameter)	1 × 10^6 cells/mL ‡NFRD	1 kHz & 100 kHz §NSVD 10 μm × 10 μm	Extracted Properties (Young's modulus, electrical diameter, C_{mem} & σ_{cyt}); Equivalent Circuit Models	Wang *et al.* 2017[156]
Model Cell Lines	Characterization of deformability and impedance phenotypes of cancer cells	Model MCF-7 cell line (~15-25 μm cell diameter)	>430 cells/min	50 kHz 2 V amplitude 10 μm × 20 μm	Transit-time, Magnitude; Neural Network Pattern Recognition (three-layer back propagation)	Yang *et al.* 2019[115]
Model Cell Lines	Viability assessment of drug-treated cancer cells	Model T47D cell line (~10–20 μm cell diameter)	4 × 10^5 cells/mL ‡NFRD	500 kHz & 300 kHz to 30 MHz (4 simultaneous frequencies); §NSVD 100 μm × 30 μm	Magnitude, Phase; Neural Network Pattern Recognition (support vector machines)	Ahuja *et al.* 2019[53]
Pollen	Viability assessment of pollen	Tobacco (*Nicotiana tabacum*), tomato (*Solanum lycopersicum*), cucumber (*Cucumis sativus*) and pepper (*Capsicum Annuum*) pollen (~15–150 μm cell diameter) (testing particles: 10, 20, 30, 60 and 100 μm *PS beads)	5 x 10^{4-5} cells/mL 1-5 × 10^4 beads/mL ‡NFRD	500 kHz, 3 MHz & 12 MHz §NSVD 120-250 μm × 120-250 μm	Magnitude & Phase	Heidmann *et al.* 2016[169]
Red Blood Cells	Characterization of phenotypical properties of individual RBCs	RBCs, sphericallized RBCs, RBCs ghosts (~7.5 μm × 2 μm) (ref. particles: 7 μm *PS beads)	5 × 10^5 cells/mL 40 μL/min	18 MHz & 250 kHz to 80MHz (8 simultaneous frequencies) 4 V amplitude 40 μm × 30 μm	Real, Imaginary, Magnitude, Phase & Dielectric Properties (Electrical Radius, C_{mem}, ε_{cyt} & σ_{cyt}); Multi-shell Modelling	Spencer & Morgan 2020[89]
Stem Cells	Characterization of phenotypical properties of skeletal stem cells after enrichment and expansion	Patient-derived skeletal stem cells & human bone marrow mononuclear cells – hBMMNCs (~5–30 μm cell diameter); (ref. particles: 7 μm *PS beads	2-2.5 × 10^5 cells/mL 0.5-1 × 10^5 beads/mL 40 μL/min	500 kHz & 2 MHz 4 V amplitude 40 μm × 30 μm	Electrical diameter, Opacity (Magnitude 2MHz / Magnitude 500 kHz) & Fluorescence	Xavier *et al.* 2017[161]
White Blood Cells	Detection and profiling of activated T-lymphocytes	Unstimulated $CD8^+$ T-lymphocytes, activated $CD8^+$-$CD69^+$ T-lymphocytes, non-activated $CD8^+$-$CD69^-$ T-lymphocytes (~5–15 μm cell diameter); (ref. and testing particles: 8, 10 and 15 μm *PS beads)	3-5 × 10^5 cells/mL 5 × 10^5 beads/mL 1 μL /min 400 cells/min	100 kHz to 27 MHz (6 simultaneous frequencies) 0.4 V amplitude 30 μm × 50 μm	Real & Imaginary	Rollo *et al.* 2017[79]
White Blood Cells	Detection and profiling of white blood cells post inertial-based separation	Lymphocytes, monocytes and neutrophils (~5–20 μm cell diameter); (testing particles: diluted whole blood and peripheral blood mononucleated cells)	1 × 10^6 cells/mL 5 μL /min	300 kHz & 1.7 MHz 3 V amplitude 30 μm × 20 μm	Magnitude & Opacity (Magnitude 1.7 MHz / Magnitude 300 kHz)	Petchakup *et al.* 2018[60]
White Blood Cells	Detection and profiling of neutrophils post integrated inertial-based separation of white blood cells	Lymphocytes, monocytes and neutrophils (testing particles: peripheral blood mononucleated cells) (~5–20 μm cell diameter); (ref. particles: 10 μm *PS beads)	1-5 × 10^5 cells/mL 1-2.5 × 10^4 beads/mL ~800 cells/min	300 kHz & 1.7 MHz §NSVD 30 μm × 20 μm	Electrical diameter & Opacity (Magnitude 1.7 MHz / Magnitude 300 kHz)	Petchakup *et al.* 2019[63]
White Blood Cells	Characterization of deformability and impedance phenotypes of diabetic lymphocytes	Normal and diabetic-activated lymphocytes (~5–15 μm cell diameter); (testing particles: normal and fixed RBCs)	4 × 10^6 cells/mL 50 μL /h	800 kHz 0.1 V amplitude 10 μm × 5-15 μm	Transit-time & Magnitude	Mahesh *et al.* 2019[145]
Yeast Cells	Viability assessment of drug-treated yeast cells and insect cells	Yeast cells (*Saccharomyces cerevisiae carlsbergensis*) (~4–40 μm cell diameter); Normal and baculovirus-infected *Sf9* insect cell	1 × 10^{5-7} cells/mL 500 to 1000 cells/s	500 kHz, 10 MHz & 12 MHz §NSVD 30-50 μm × 30-50 μm	Magnitude & Phase	Opitz *et al.* 2019[72]
Yeast Cells	Detection and cell shape phenotyping of single budding yeast cells	Budding yeast cells (*Saccharomyces cerevisiae*) (~4–40 μm cell diameter); (testing particles: 5 and 8 μm *PS beads; 8 and 15 μm by 4 μm SU-8 rods)	10^7 cells/mL 40 μL/min ~3–6 cells/s	1 MHz 0.2 V amplitude 17 μm × 12 μm	Particle shape metrics & Magnitude;	Xie *et al.*2019[88]
Yeast Cells	Dielectrophoretic trapping and determination of cell size	Budding yeast cells (*Saccharomyces cerevisiae*) (~4–40 μm cell diameter); (testing particles: 6, 8 and 10 μm *PS beads)	1 × 10^6 cells/mL 1 × 10^{5-6} beads/mL 0.5 μL/min	300 kHz to 10 MHz §NSVD 150 μm × 15 μm	Magnitude	Geng *et al.* 2019[132]

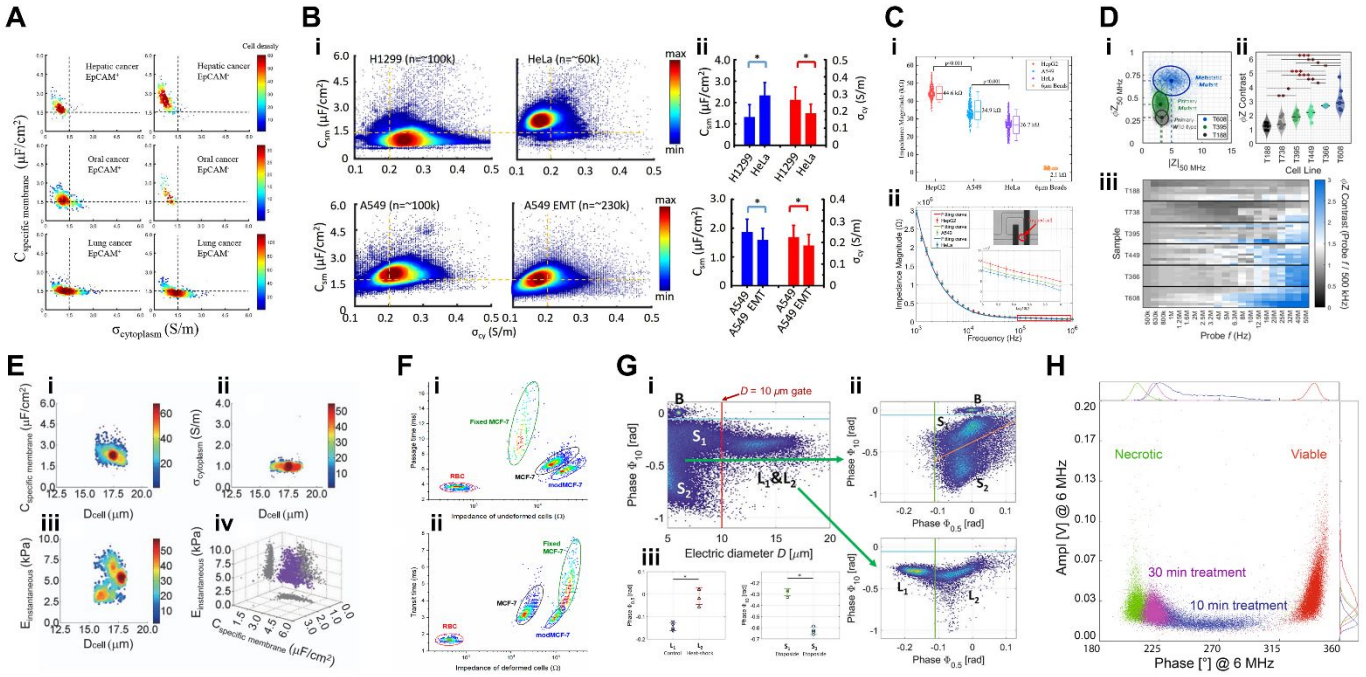

Fig. 6 Collection of phenotyping results on cancer cells and model cell lines from literature. See Sections 4.1, 4.2 and 4.3 for further details. (A) Measurements of estimated σ_{cyt} vs C_{mem} of CTCs, with and without EpCAM expression, from hepatic, oral and lung cancers. (B) i - Measurements of estimated σ_{cyt} vs C_{mem} of H1299, HeLa, A549 and A549 undergoing EMT (epithelial mesenchymal transition); ii – comparison between cell lines, where significant differences were observed ($*p <$ 0.001). (C) i – Impedance magnitude distributions for three cancer types and reference beads; ii – EIS magnitude measurements of the three cancer types with corresponding MMT model fitting curves. (D) i – Measurements of impedance magnitude vs phase at 50 MHz for various PDAC cell lines; ii – comparison of impedance phase contrast between cell lines, where significant differences were observed ($*p <$ 0.003, $**p <$ 0.0007, $***p <$ 0.00007); iii – Phase contrast range for PDAC samples along the frequency spectra measured. (E) Measurements of 95D model cells in terms of their estimated: i - D_{cell} vs C_{mem}; ii - D_{cell} vs σ_{cyt}; iii - D_{cell} vs $E_{instantaneous}$; iv - C_{mem} vs σ_{cyt} vs $E_{instantaneous}$. (F) Measurements of impedance vs transit time for cells before (i) and after (ii) passing the channel constriction. (G) i - Measurements of electric diameter vs impedance phase at 10 MHz for U937 model cells containing untreated and heat-treated cells; ii – Measurements of impedance phase at 0.5 MHz vs impedance phase at 10 MHz for gated sub-populations of smaller (top) and bigger (bottom) size; iii – comparison of impedance phase at 0.5 MHz (left) and 10 MHz (right) between the identified subpopulations, where significant differences were observed ($*p <$ 0.001). (H) Measurement of impedance phase vs magnitude at 6MHz of U937 model cells undergoing a NM-300k treatment. Images were adapted with permission from (A) ref. [162], copyright 2017 Elsevier B.V., (B) ref. [154], copyright 2018 Elsevier B.V., (C) ref. [129], copyright 2019 American Chemical Society, (D) ref. [71], copyright 2020 Elsevier B.V., (E) ref. [156], copyright The Author(s) 2017, (F) ref. [116], copyright 2018 American Chemical Society, (G) ref. [64], copyright 2020 Elsevier B.V., (H) ref. [41], copyright The Author(s) 2020.

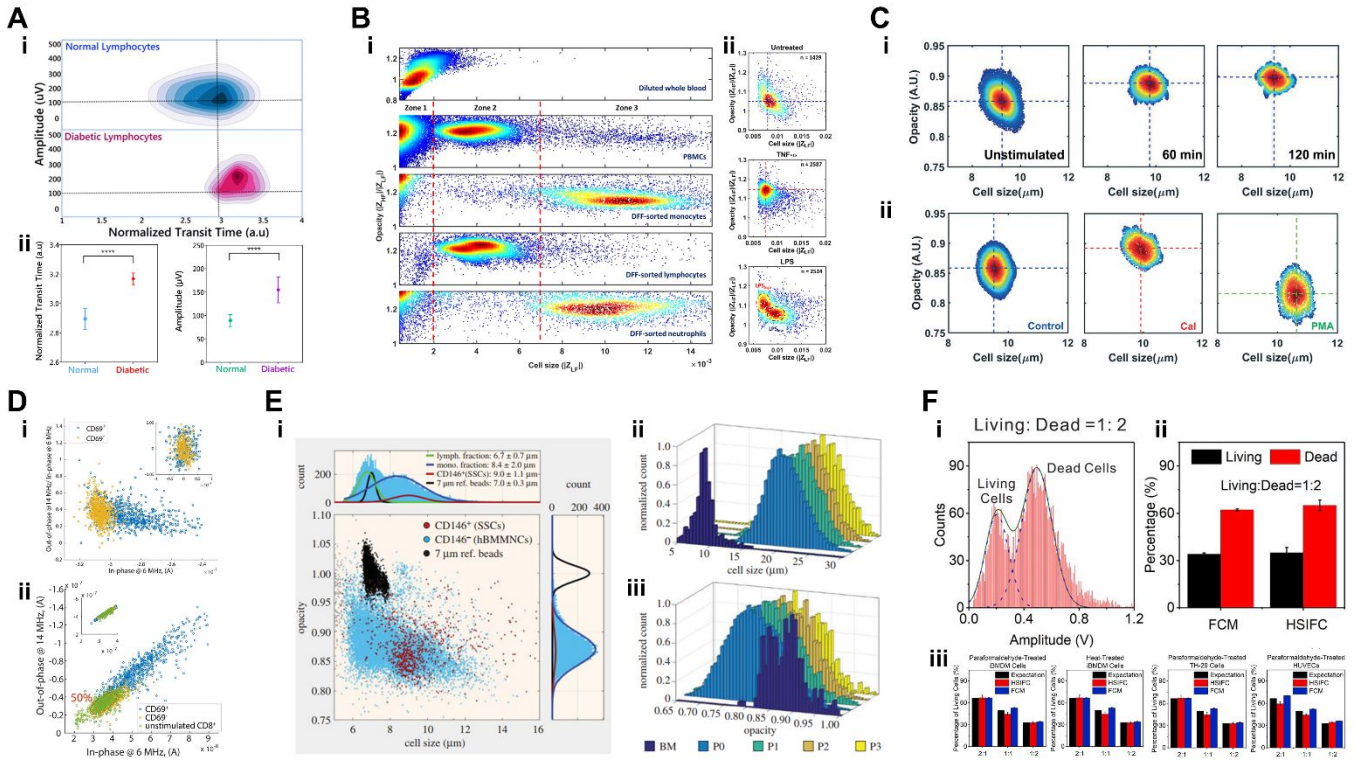

Fig. 7 Collection of phenotyping results on mammalian cells from literature. See Sections 4.4 for further details. (A) i – Measurements of transit time vs signal amplitude for normal and diabetic lymphocytes; ii – comparison of transit time (left) and signal amplitude (right) between normal and diabetic lymphocytes, where significant differences were observed (****$p <$ 0.0001). (B) Measurements of impedance magnitude at 300 kHz vs opacity (impedance magnitude at 1.7 MHz / 300 kHz) for various cell populations; ii - Measurements of impedance magnitude at 300 kHz vs opacity (impedance magnitude at 1.7 MHz / 300 kHz) for untreated, TNF-α and LPS treated monocytes. (C) Measurements of electrical size vs opacity (impedance magnitude at 1.7 MHz / 300 kHz) for: i – neutrophils undergoing NETosis at different time points; ii – neutrophils undergoing NETosis induced via Cal and PMA. (D) Measurements of in-phase vs out-of-phase signals at 6 MHz (i) and 14 MHz (ii) for $CD69^+$ and $CD69^-$ T-lymphocytes (i) and unstimulated $CD8^+$, $CD69^+$ and $CD69^-$ T-lymphocytes (ii). (E) i – Measurements of electrical size vs opacity (impedance magnitude at 2 MHz / 500 kHz) for $CD146^+$ and $CD146^-$ hBMMNCs; and distributions of electrical size (ii) and opacity (ii) for SSCs along passage number for one individual patient. (F) i – Distribution of signal amplitude at 450 kHz for a population of live an dead iBMDM cells; ii – comparison between viability estimations by flow cytometry (FCM) and impedance cytometry (HSIFC); iii – comparison between viability estimations by FCM and HSIFC for various cell types and treatments. Images were adapted with permission from (A) ref. [145], copyright 2019 IOP Publishing, (B) ref. [60], copyright 2018 Elsevier B.V., (C) ref. [63] copyright 2019 The Royal Society of Chemistry, (D) ref. [79], copyright 2017 Elsevier B.V., (E) ref. [161], copyright 2017 The Royal Society, (F) ref. [119], copyright 2020 Elsevier B.V..

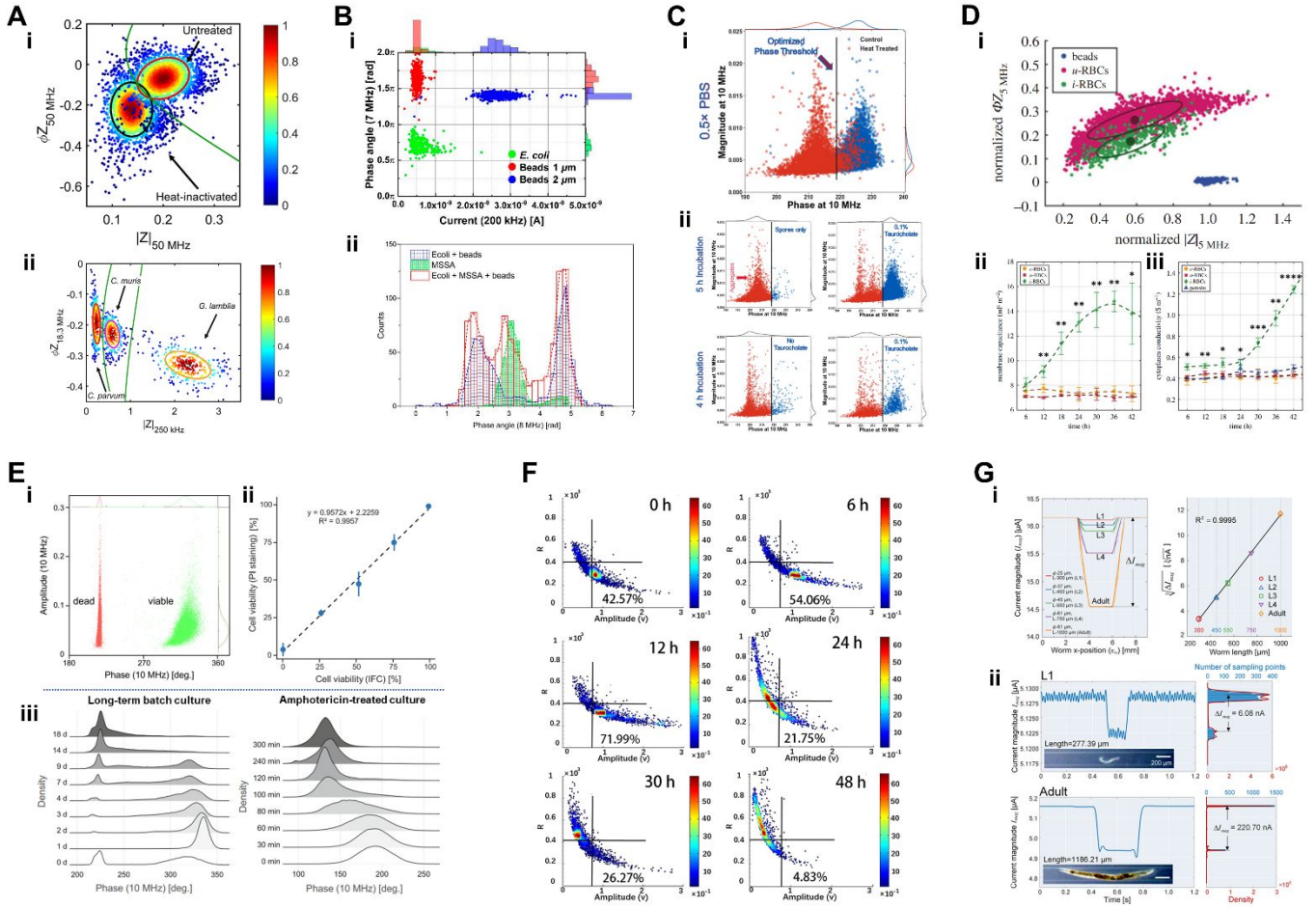

Fig. 8 Collection of phenotyping results on various sample types from literature. See Sections 4.5, 4.6 and 4.7 for further details. (A) i - Measurements of impedance magnitude vs impedance phase at 50MHz for untreated and heat-treated *C. parvum* oocysts; ii - measurements of impedance magnitude at 250 kHz vs impedance phase at 18.3MHz for different waterborne pathogens. (B) i – Measurements of current at 200 kHz vs impedance phase at 7MHz for *E. coli* and reference beads; ii – distribution of impedance phase at 8 MHz for populations of bacteria and reference beads. (C) Measurement of impedance phase vs impedance magnitude at 10 MHz for: i - untreated and heat-treated *C. difficile*; ii – *C. difficile* cells under various conditions to quantify spore germination. (D) i – Measurement of impedance magnitude vs impedance phase at 5 MHz for a mixed population of reference beads and uninfected and malaria parasite infected-RBCs; and estimated alterations to C_{mem} (ii) and σ_{cyt} (iii) for each cell population based on multi-shell modelling. (E) i – Measurement of impedance phase vs impedance magnitude at 10 MHz for untreated (viable) and heat-treated (dead) yeast cells; ii – comparison between viability estimations by impedance cytometry vs flow cytometry for various mixed samples of viable and dead yeast cells; iii – distributions of impedance phase at 10 MHz for yeast cells for long-term viability analysis. (F) Measurements of impedance magnitude at 1 MHz vs a particle shape metric R for budding and single yeast cells along the culturing process. (G) i – Simulations of current magnitude for *C. elegans* worms at five developmental stages (L1-L4 and adult); ii – measurements of current magnitude for exemplary *C. elegans* worms at L1 and adult developmental stage. Images were adapted with permission from (A) ref. [151], copyright The Author(s) 2017, (B) ref. [40], copyright 2018 Multidisciplinary Digital Publishing Institute, (C) ref. [153], copyright 2020 Elsevier B.V., (D) ref. [69], copyright 2018 The Royal Society, (E) ref. [72], Springer-Verlag GmbH Germany, part of Springer Nature 2019. (F) ref. [88], copyright 2019 American Chemical Society, (G) ref. [108], copyright 2018 Elsevier B.V..

Table 3 Key phenotypical findings using single-cell microfluidic impedance cytometry

Cell Phenotype of Interest	Dielectric Property	Sub-cellular Properties
Cell Death: viable, necrotic and apoptotic	C_{mem}	Loss of viability, e.g. induced by heat-inactivation, causes increased cell membrane permeability with break-down of the membrane integrity, rendering cells non-viable. These result in a decreased C_{mem}, as the cell loses the ability to function as a perfect insulator at low frequencies. Such phenomena have been observed in literature: heat-treated non-viable MCF7 cells show higher magnitude opacity (i.e. lower C_{mem}) than viable cells in 1× PBS (ref. [160]); heat-treated non-viable lymphoma cells show a decrease in absolute impedance phase at 500 kHz in 1× PBS (ref. [64]); heat-treated non-viable algae cells show a decrease in magnitude opacity (based on 20 MHz / 500 kHz data) in 1× PBS (ref. [55]); cytotoxic nanomaterials-induced non-viable lymphoma cells show lower impedance phase at 6 MHZ in a 0.25xPBS + sucrose buffer (ref. [41]); hypertonic stimulus-induced non-viable HUVECs show increased impedance magnitude at low frequency (450 kHz) (ref. [119]);
	σ_{int} & ε_{int}	Increased permeability in non-viable cells causes increased ion exchange between the cell interior and medium, together with internal degradation of cell organelles. These result in alterations of the cell interior properties, such as σ_{int} & ε_{int}, which can be qualitatively observed with changes to impedance at higher frequencies, as reported in literature: heat-treated non-viable yeast cells show a decrease in impedance phase at 10 MHz in 0.5× PBS (ref. [72]); heat-treated non-viable pollen particles show a decrease in impedance phase at 12 MHz (ref. [169]); apoptosis causes shedding of smaller-sized apoptotic bodies from cells, identifiable based on their size and greater impedance phase at high frequency (≥10 MHz) in 1× PBS (ref. [64]);
Immune Cells: cell activation, differentiation and diabetic response	Size & C_{mem}	Monocytes, lymphocytes and neutrophils are distinguishable based on impedance magnitude and opacity (refs. [60,195,196]). When processes such as activation or differentiation occur in these cell types, alterations to cell membrane permeability and conformation can result in alterations to C_{mem}. Various phenomena have been reported in literature: monocyte differentiation into macrophages results in size increase but no impedance magnitude alteration (ref. [60]); inflammatory stimulus induces an increase in impedance magnitude opacity (i.e. lower C_{mem}) (ref. [60]); NETosis neutrophils have higher cell size and magnitude opacity (i.e. lower C_{mem}) than unstimulated neutrophils (ref. [63]); diabetic lymphocytes present loss of deformability and higher impedance magnitude at 800 kHz than normal lymphocytes (ref. [145]); diabetic neutrophils show higher magnitude opacity (i.e. lower C_{mem}) than monocytes in 1× PBS (ref. [60]); glucose-stimulated neutrophils show larger size than unstimulated neutrophils at 120 min post-stimulus (ref. [63]);
Cancer Cells: measuring drug sensitivity & metastasis	C_{mem} & σ_{cyt}	Cancer cells are known for an increased cell membrane roughness and folding, which affects the surface area dependent metric of C_{mem}, and higher nucleus-to-cytoplasm ratios and cell cycle turnover, which in turn affects estimations of σ_{cyt}. Differences in the phenotypes of various cancer cells tied to these specific characteristics have been reported in literature: EpCAM+ CTCs have lower C_{mem} and higher σ_{cyt} than EpCAM- CTCs (ref. [162]); epithelial-mesenchymal transitions (EMT) on lung tumour cells causes lower C_{mem} and σ_{cyt} (ref. [154]); lung metastasis adenoid carcinoma cells present a lower C_{mem} and higher σ_{cyt} than non-metastatic adenoid carcinoma cells (ref. [163]); more tumourigenic pancreatic cancer cells show higher impedance phase at high frequencies (>10 MHz) and lowered σ_{int} (ref. [71]);
Bacteria: detection, viability, germination and antibiotic susceptibility	σ_{int} & ε_{int}	Gram-negative *E. coli* and Gram-positive *S. aureus* are detectable and discriminated using impedance phase at 8 MHz with a buffer of low conductivity (0.085 S/m) (ref. [40]); Heat-treated *C. difficile* bacteria show lower impedance phase at 10 MHz than untreated bacteria (ref. [153]); Germinated vegetative *C. difficile* bacteria have higher impedance phase at 10 MHz than *C. difficile* in spore form (ref. [153]);
Stem Cells: alterations with cell expansion and passage	Size & C_{mem}	Unexpanded skeletal stem cells are larger than other bone marrow cell populations (ref. [161]), while the expansion of skeletal stem cells and following passages cause an increase in size and C_{mem} (assessed by magnitude opacity) (ref. [161]);

Review of chip designs and data analytics to stratify heterogeneity in cellular systems via microfluidic impedance cytometry

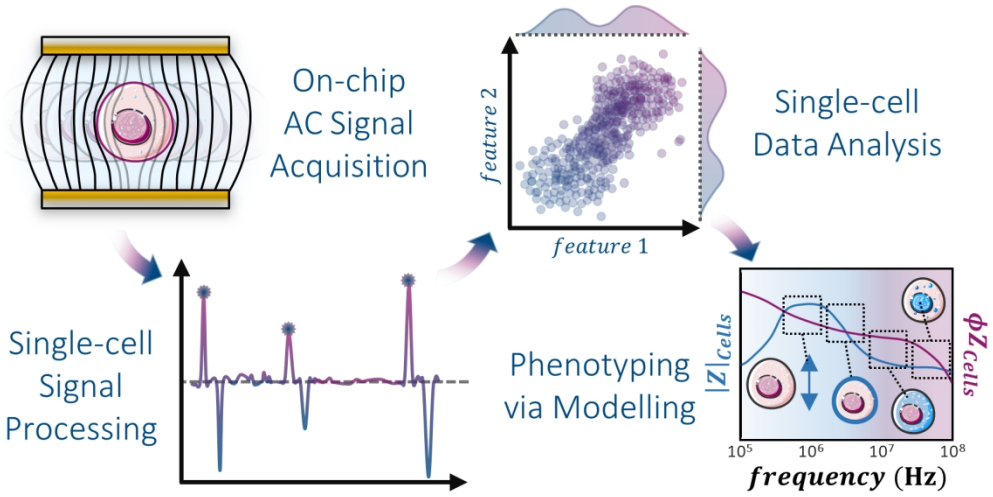
On-chip
AC Signal
Acquisition
feature 2
feature 1
Single-cell
Data Analysis
Single-cell
Signal
Processing
Phenotyping
via Modelling
|Z|Cells
ΦZCells
10^5
10^6
10^7
10^8
frequency (Hz)